Ketamine alleviates NMDA receptor hypofunction through synaptic trapping

Graphical abstract
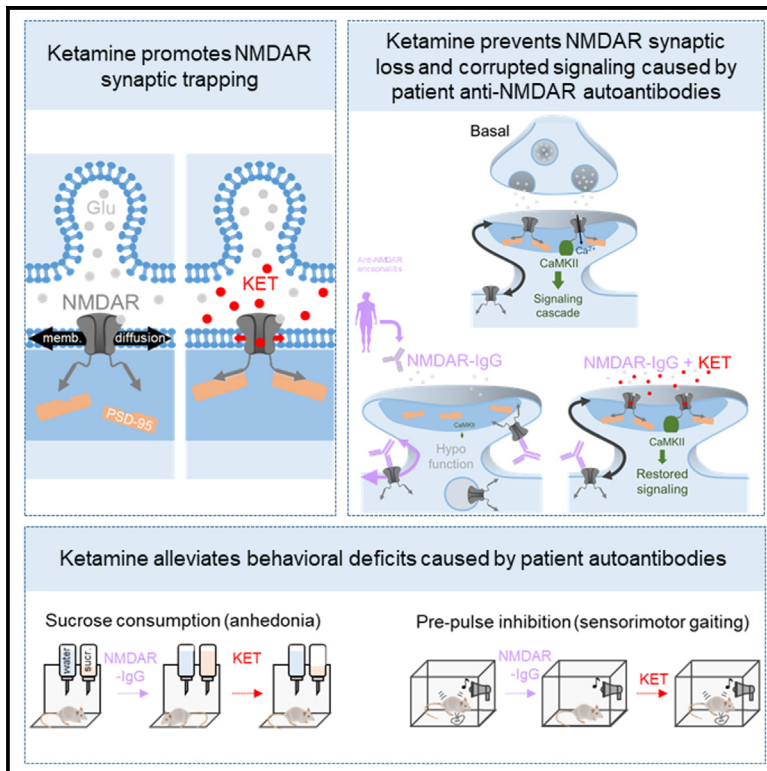
Authors

Frédéric Villéga, Alexandra Fernandes, Julie Jézéquel, ..., Jérôme Honnorat, Julien P. Dupuis, Laurent Groc

Correspondence

julien.dupuis@u-bordeaux.fr (J.P.D.), laurent.groc@u-bordeaux.fr (L.G.)

In brief

Villéga, Fernandes, Jézéquel et al. report that NMDAR open channel blockers, such as ketamine, favor receptor trapping at excitatory synapses through enhanced interactions with scaffolding proteins. They further show that ketamine-elicited trapping enhancement alleviates NMDAR synaptic impairments and behavioral deficits caused by autoantibodies from patients with anti-NMDAR encephalitis.

Highlights

- Open channel blockers (OCBs) such as ketamine promote NMDAR synaptic trapping

- OCB binding enhances interactions between NMDARs and scaffolding proteins

- Ketamine prevents NMDAR depletion at synapses exposed to anti-NMDAR autoantibodies

- Ketamine alleviates behavioral deficits provoked by anti-NMDAR autoantibodies

CellPress

Neuron

Article

Ketamine alleviates NMDA receptor hypofunction through synaptic trapping

Frédéric Villéga,[1,2,5] Alexandra Fernandes,[1,5] Julie Jézéquel,[1,5] Floriane Uyttersprot,[1] Nathan Benac,[1] Sarra Zenagui,[1] Laurine Bastardo,[1] Hélène Gréa,[1] Delphine Bouchet,[1] Léa Villetelle,[1] Olivier Nicole,[1] Véronique Rogemond,[3,4] Jérôme Honnorat,[3,4] Julien P. Dupuis,[1,*] and Laurent Groc[1,6,*]

[1]University of Bordeaux, CNRS, Interdisciplinary Institute for Neuroscience, IINS UMR 5297, 33000 Bordeaux, France
[2]Department of Pediatric Neurology, CIC-1401, University Children's Hospital of Bordeaux, Bordeaux, France
[3]Synaptopathies and Autoantibodies Team, Institut NeuroMyoGene-MeLis, INSERM U1314, CNRS UMR 5284, Université Claude Bernard Lyon1, 69373 Lyon, France
[4]French Reference Centre on Paraneoplastic Neurological Syndromes and Autoimmune Encephalitis, Hospices Civils de Lyon, Hôpital Neurologique Pierre Wertheimer, 69677 Bron, France
[5]These authors contributed equally
[6]Lead contact
*Correspondence: julien.dupuis@u-bordeaux.fr (J.P.D.), laurent.groc@u-bordeaux.fr (L.G.)
https://doi.org/10.1016/j.neuron.2024.06.028

SUMMARY

Activity-dependent modulations of N-methyl-D-aspartate glutamate receptor (NMDAR) trapping at synapses regulate excitatory neurotransmission and shape cognitive functions. Although NMDAR synaptic destabilization has been associated with severe neurological and psychiatric conditions, tuning NMDAR synaptic trapping to assess its clinical relevance for the treatment of brain conditions remains a challenge. Here, we report that ketamine (KET) and other clinically relevant NMDAR open channel blockers (OCBs) promote interactions between NMDAR and PDZ-domain-containing scaffolding proteins and enhance NMDAR trapping at synapses. We further show that KET-elicited trapping enhancement compensates for depletion in synaptic receptors triggered by autoantibodies from patients with anti-NMDAR encephalitis. Preventing synaptic depletion mitigates impairments in NMDAR-mediated CaMKII signaling and alleviates anxiety- and sensorimotor-gating-related behavioral deficits provoked by autoantibodies. Altogether, these findings reveal an unexpected dimension of OCB action and stress the potential of targeting receptor anchoring in NMDAR-related synaptopathies.

INTRODUCTION

The vast majority of fast excitatory transmission between nerve cells occurs through the synaptic release of glutamate and subsequent activation of post-synaptic ionotropic AMPA, kainate, and N-methyl-D-aspartate (NMDA) glutamate receptors (NMDARs). NMDAR functions encompass the regulation of neuronal migration, synaptogenesis and maturation during development, and the initiation of long-term synaptic plasticity and fine-tuning of brain network activities and behaviors.[1] NMDARs are tetrameric receptors incorporating two obligatory GluN1 subunits, which bind the co-agonists glycine or D-serine, and two glutamate-binding GluN2(A-D) or, less commonly, glycine-binding GluN3(A-B) subunits.[2] These complexes form glutamate-gated ion channels permeant to sodium, potassium, and calcium, contributing to post-synaptic depolarization and initiating activity-dependent changes in synapse structure and function. Although NMDAR-mediated calcium influxes allow the recruitment of proteins that are essential for adaptive cellular processes,[2] an increasing corpus of studies unveils that

NMDAR-dependent functions also involve mechanisms that do not require their ion channel features.[3,4] As such, non-ionotropic signaling[5,6] participates in structural plasticity and diffusion-based surface redistributions control the amount, composition, and organization of synaptic receptors and allow the recruitment of protein kinases to post-synaptic densities (PSDs).[7,8] Thus, NMDAR-mediated signaling relies on a complex mosaic of ionotropic, non-ionotropic, and trafficking-based processes.

Consistent with their crucial role in cell communication, NMDAR dysfunctions have been associated with some of the most devastating human pathologies, including cancer, diabetes, and brain diseases. NMDARs expressed by cancer cells contribute to tumor growth and brain metastasis,[9,10] while pancreatic NMDARs on β cells are putative targets to regulate insulin secretion.[11] In the brain, NMDAR dysfunctions have long been suspected to participate in neurological and psychiatric disorders such as Alzheimer's disease, depression, stroke, epilepsy, and schizophrenia,[1,2] based on genetic mutations found in patients and pharmacological studies showing that activating or

antagonizing NMDARs can mimic core symptoms of these illnesses. However, direct evidence for a central contribution of NMDAR dysfunctions in brain disorders only recently emerged from the description of anti-NMDAR encephalitis[12] in which patients develop autoantibodies directed against an extracellular N-terminal domain of the obligatory GluN1 subunit (NMDAR-immunoglobulin G [IgG]).[13] Clinically, patients suffer from cognitive deficits, major psychiatric symptoms (e.g., psychosis), seizures, abnormal movements, and other clinical presentations,[14] all of which can be ameliorated through immunotherapy that allows the removal of pathogenic NMDAR-IgG and the functional resetting of synapses and neuronal network functions.[13,15–17] From a mechanistic point of view, NMDAR-IgG do not harm NMDAR channel properties but cause their synaptic destabilization and disorganization at the plasma membrane.[16–19] Over time, these impairments disrupt α-amino-3-hydroxy-5-methyl-4-isoxazolepropionic acid receptor (AMPAR)- and gamma-aminobutyric acid receptor (GABA$_A$R)-mediated neurotransmissions, leading to an excitation/inhibition imbalance that alters network activity and promotes oscillations.[20,21] These discoveries marked a significant step forward in our understanding of the mechanisms underpinning NMDAR contributions to the etiology of brain disorders. However, despite intense efforts from academic and private actors, therapeutic attempts to counteract NMDAR dysfunction using compounds modulating NMDAR activity have yielded rather disappointing outcomes so far.[22–25]

Common explanations include the fact that targeting NMDAR channel properties often comes with major adverse effects, and NMDAR agonists and antagonists elicit a variety or responses at the synaptic, network, and behavioral levels.[2] For instance, open channel blockers (OCBs) induce behavioral responses that are not observed with competitive antagonists, suggesting that they affect different dimensions of NMDAR signaling.[26] Among OCBs, ketamine (KET) has sparked sustained attention from physicians and neuroscientists over the past decades. Depending on the dose, KET exhibits powerful anesthetic or psychoactive properties, including an unmatched ability to alleviate the symptoms of treatment-resistant depression upon a single administration.[27] However, the molecular mechanisms supporting these therapeutic attributes remain misunderstood and appear not to rely on its pore-blocking capacities only as they cannot be replicated by other NMDAR antagonists. Recently, surface diffusion-based spatiotemporal rearrangements in the organization and trapping of NMDAR at synapses has emerged as a key regulatory mechanism controlling the initiation of activity-dependent synaptic adaptations supporting cognitive functions.[7,8,28] These discoveries prompted us to investigate whether specific subclasses of NMDAR antagonists may act upon NMDAR trafficking and trapping at synapses. Here, we demonstrate that OCB binding induces conformational rearrangements promoting interactions between NMDAR and PDZ domain-containing scaffolding proteins, resulting in enhanced trapping of the receptors at synapses. Furthermore, we show that enhanced trapping elicited by OCBs compensates for depletion in synaptic receptors caused by NMDAR-IgG, thereby restoring Ca^{2+}/calmodulin-dependent protein kinase II (CaMKII) signaling and alleviating behavioral deficits provoked by patient autoantibodies. These data suggest that the action of OCBs on brain functions may involve the promotion of NMDAR synaptic trapping.

RESULTS

Open channel blockers enhance the synaptic trapping of NMDAR

NMDAR synaptic trapping is ensured by a complex combination of extracellular, transmembrane, and cytosolic protein-protein interactions finely tuned through post-translational modifications and binding of ligands, such as NMDAR agonists and co-agonists.[29] Based on these discoveries, we examined whether, like receptor activation, inhibition might impact NMDAR trapping and organization at excitatory synapses. To do so, we compared the actions of several classes of NMDAR antagonists with therapeutical interest, i.e., the competitive antagonist D-2-amino-5-phosphonovalerate (D-AP5), the glycine-binding site antagonist kynurenic acid (KA), and the uncompetitive OCBs dizocilpine (MK-801), KET, and memantine (MEM) (Figure 1A). Although all of them exhibited comparable inhibition of NMDAR-mediated calcium influx in hippocampal cultured neurons (Figures S1A and S1B), single-particle tracking (SPT) revealed that a 1-h exposure to KET and MK-801 strongly reduced the surface diffusion and enhanced the confinement of endogenous NMDAR at synapses, thereby increasing their synaptic residency time (Figures 1B–1G; Figures S1C–S1G). It is noteworthy that similar results were obtained in the presence of tetrodotoxin (TTX) following an acute (5 min) co-application of the drugs with NMDA to allow OCB action despite the absence of action potential firing (Figures 1H–1J; Figures S1H–S1J), showing that enhanced receptor trapping does not result from a drop in network activity caused by the antagonists but arises from a direct action of the drugs on the receptors. These observations were further confirmed using photoactivated localization microscopy (PALM) to track GluN1-mEos3.2-NMDAR before and 5 min after exposure to the drugs co-applied with NMDA in the presence of TTX (Figure S2). Interestingly, MEM enhanced receptor confinement at synapses in these experimental conditions (Figures S2B and S2C), suggesting that it might also provoke some intermediate level of receptor trapping. Extrasynaptic receptors remained unaffected by OCBs whatever the experimental configuration (Figure S2C). We then assessed whether OCBs also affect the synaptic behavior of other transmembrane proteins. Neither the diffusion nor the residency time at excitatory synapses of EphB2 tyrosine kinase receptors (EphB2Rs) or voltage-gated potassium channels K$_V$1.3 were affected by prolonged exposure to KET (Figures S3A and S3B). Likewise, the diffusion, residency time and surface explored by γ2 subunit-containing GABA$_A$ receptors at inhibitory synapses remained unaffected after acute exposure to KET co-applied with NMDA in the presence of TTX (Figures S3C–S3F). Together, these results demonstrate that OCBs selectively enhance the trapping of NMDAR at excitatory synapses.

Acute exposure to OCBs has a limited impact on NMDAR synaptic numbers and organization

We next assessed whether enhanced receptor trapping caused by OCBs alters the amount and distribution of NMDAR at

CellPress
OPEN ACCESS
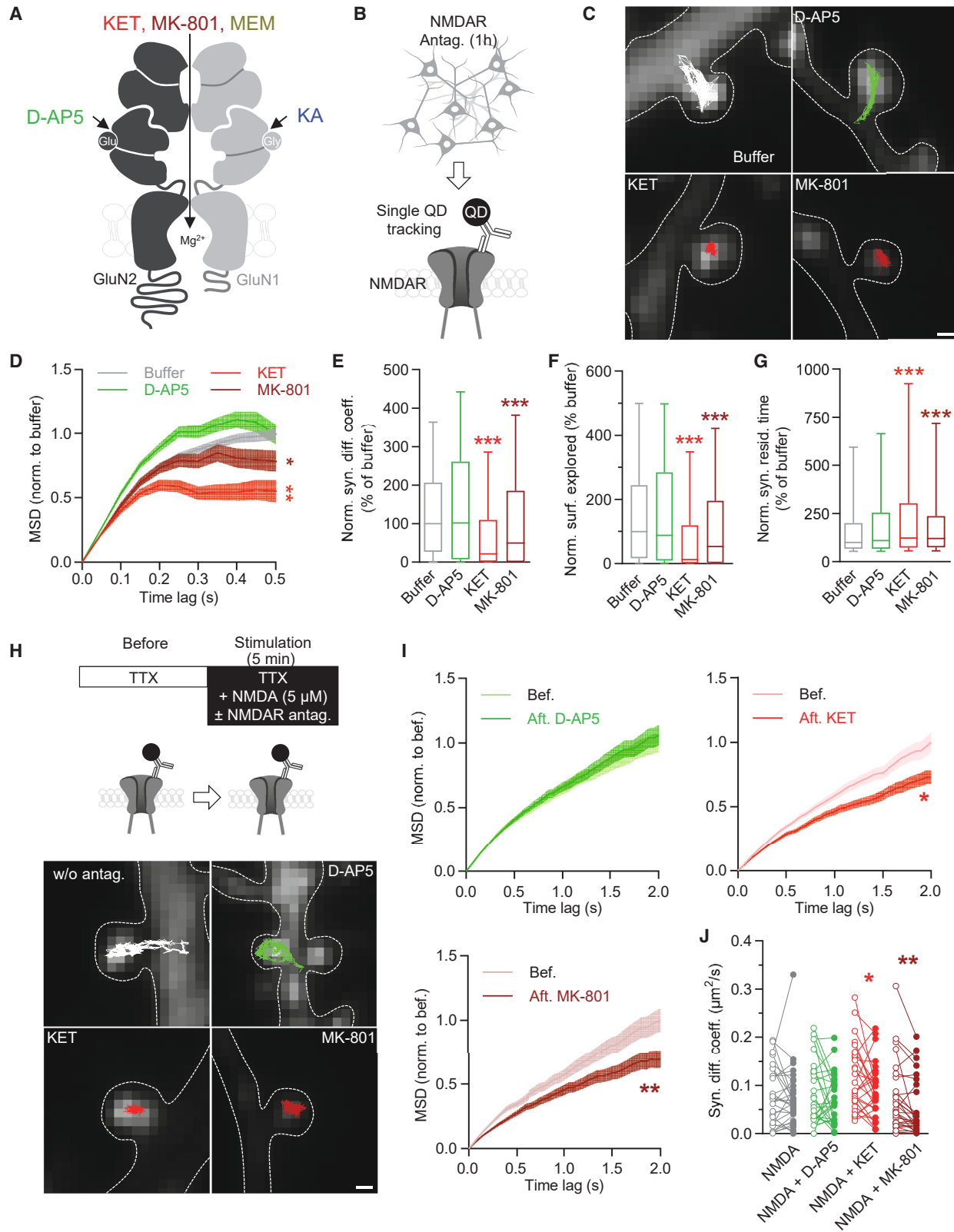
(legend on next page)

synapses. None of the drugs modified the number of dendritic spines after a 1-h exposure (Figures S4A and S4B). Accordingly, the linear density of NMDAR clusters and their macroscopic features remained unchanged (Figures 2A and 2B; Figures S4C–S4E), suggesting that acute exposure to NMDAR antagonists does not affect the number of receptors at synapses. Rearrangements of NMDAR synaptic organization and subsequent signaling adjustments may occur without obvious changes in the number of synaptic receptors.[8] Thus, we examined this possibility using stochastic optical reconstruction microscopy (STORM), a single-molecule localization microscopy approach that can provide the nanoscale map of surface NMDAR. Interestingly, a 1-h exposure to D-AP5 caused a significant contraction and an increase in the density of synaptic NMDAR clusters and nanodomains (Figures 2C–2E). This reorganization likely resulted from an inhibition of neuronal activity triggered by D-AP5, as TTX exhibited a similar action on NMDAR clusters (Figures 2D and 2E). On the contrary, neither KET nor MK-801 affected NMDAR synaptic cluster properties. To note, MEM did not affect the size or density of NMDAR synaptic clusters and nanodomains (Figures S4F and S4G). Altogether, these data indicate that short-term exposure to OCBs increase NMDAR synaptic trapping and thus prevent activity-dependent receptor reorganizations.

KET drives conformational changes in NMDAR cytosolic domains and favors synaptic trapping through enhanced interaction with PDZ domain scaffolding proteins

NMDAR trapping at excitatory synapses involves a variety of interactions with intracellular proteins.[29] Thus, we investigated whether OCBs would enhance NMDAR synaptic stabilization by modulating interactions with its cytosolic partners. For this, we used fluorescence lifetime imaging of Förster resonance energy transfer (FLIM-FRET) between GluN1 C termini as a proxy for their conformation.[30,31] We first explored whether the binding of antagonists changes the conformation of NMDAR cytosolic domains. In hippocampal neurons expressing recombinant NMDAR incorporating GFP- and mCherry-tagged GluN1 subunits (Figure 3A), we monitored evolutions in GFP lifetime before and 5 min after co-exposure to NMDA (5 µM) and antagonists as a proxy for conformational changes in the cytosolic domains of the receptors.[31,32] None of the experimental conditions affected GFP fluorescence lifetimes in NMDAR clusters expressing GluN1-GFP alone (Figures S5A and S5B). The co-expression of the donor (GluN1-GFP) and acceptor (GluN1-mCherry) fluorophores yielded significant FRET within dendritic spine receptor clusters in all conditions (Figures 3B and 3C). Unlike D-AP5 and MEM, exposure to KET and MK-801 enhanced FRET efficiency within NMDAR clusters co-expressing GluN1-GFP and GluN1-mCherry (Figures 3B and 3C; Figures S5C and S5D). Furthermore, incorporating a point mutation (N616A) within the binding site for KET abolished the action of the drug,[33] indicating that changes in FRET efficiency proceed from drug binding to the receptors (Figures 3D–3F; Figure S5E). Together, these results indicate that the binding of KET and MK-801 drives conformational rearrangements in the cytosolic domains of NMDAR.

PDZ-domain-containing scaffolding proteins of the membrane-associated guanylate kinase (MAGUK) family are central organizers of the PSD.[34] MAGUKs are abundantly expressed at excitatory synapses, where they contribute to stabilizing NMDAR through the binding of GluN2 subunit C-terminal motifs to PDZ domains.[31,32,35] Thus, we next explored whether conformational rearrangements caused by OCBs would translate into modifications of NMDAR interactions with MAGUKs. We first examined whether disrupting interactions with MAGUKs had any impact on OCB-elicited changes in NMDAR conformation. Infusing transactivator of transcription (TAT)-conjugated

Figure 1. OCBs enhance the synaptic trapping of NMDAR

(A) Schematic representation of a GluN1/GluN2 NMDAR complex displaying the sites of action of the competitive antagonist D-2-amino-5-phosphonovalerate (D-AP5), the glycine-binding site antagonist kynurenic acid (KA), and the uncompetitive open channel blockers ketamine (KET), dizocilpine (MK-801), and memantine (MEM).

(B and C) Experimental principle (B) and epifluorescence images of dendritic segments expressing Homer1c-dsRed (gray) as a synaptic marker with representative trajectories (25 s, 20 Hz acquisition rate) of endogenous quantum dot (QD)-labeled synaptic NMDAR exposed to buffer, D-AP5 (50 µM), KET (1 µM), or MK-801 (20 µM) for 1 h (C). Scale bar, 500 nm.

(D) Normalized mean squared displacement (MSD) over time of synaptic NMDAR after 1 h exposure to buffer (gray; n = 2,580 trajectories), D-AP5 (green; n = 1,010), KET (red; n = 441), or MK-801 (wine; n = 585). Kolmogorov-Smirnov test, *p < 0.05, **p < 0.01.

(E) Normalized instantaneous diffusion coefficients of synaptic NMDAR after 1 h exposure to buffer (n = 2,631 trajectories), D-AP5 (n = 918), KET (n = 546), or MK-801 (n = 594). Data expressed as median ± 25%–75% IQR (interquartile range, box) and 10%–90% percentile (whiskers). Kruskal-Wallis followed by Dunn's multiple comparison test, ***p < 0.001.

(F) Normalized surface explored by synaptic NMDAR over 100 ms after 1 h exposure to buffer (n = 1,223 trajectories), D-AP5 (n = 491), KET (n = 205), or MK-801 (n = 296). Data expressed as median ± 25%–75% IQR (box) and 10%–90% percentile (whiskers). Kruskal-Wallis followed by Dunn's multiple comparison test, ***p < 0.001.

(G) Normalized synaptic residency time of NMDAR after 1 h exposure to buffer (n = 2,304 trajectories), D-AP5 (n = 1,321), KET (n = 735), or MK-801 (n = 861). Data expressed as median ± 25%–75% IQR (box) and 10%–90% percentile (whiskers). Kruskal-Wallis followed by Dunn's multiple comparison test, ***p < 0.001.

(H) Experimental principle (top) and epifluorescence images of dendritic segments expressing Homer1c-dsRed (gray) as a synaptic marker with representative trajectories of endogenous QD-labeled synaptic NMDAR after exposure to buffer or NMDA (5 µM) combined with D-AP5 (50 µM), KET (1 µM), or MK-801 (20 µM) in the presence of TTX (1 µM). Scale bar, 500 nm.

(I) Normalized MSD over time of NMDAR, before and after exposure to NMDA, combined with D-AP5 (before, n = 580 trajectories; after, n = 597 trajectories), KET (before, n = 464; after, n = 459), or MK-801 (before, n = 410; after, n = 433) in the presence of TTX. Kolmogorov-Smirnov test, *p < 0.05, **p < 0.01.

(J) Instantaneous diffusion coefficients of synaptic NMDAR before and after exposure to NMDA alone (n = 29 cells) or combined with D-AP5 (n = 28 cells), KET (n = 28), or MK-801 (n = 30) in the presence of TTX. Each dot represents the median diffusion coefficient for one cell, before and after treatment. Paired t test, *p < 0.05, **p < 0.01.

See also Figures S1–S3 for additional experiments related to Figure 1.
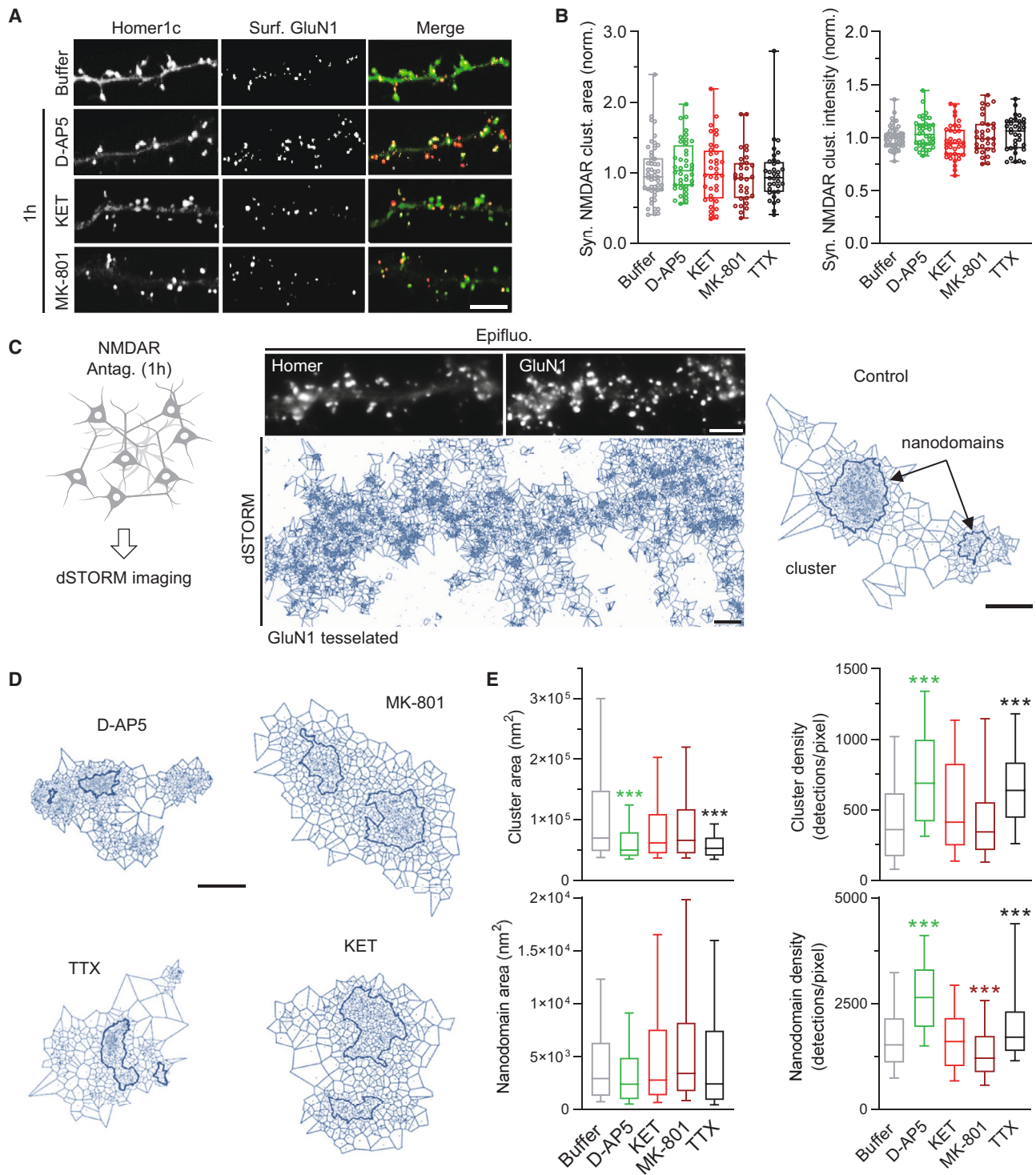
Figure 2. Acute exposure to OCBs has a limited impact on NMDAR synaptic numbers and organization

(A) Hippocampal neurons immunostained for Homer1c-GFP (green) and FLAG-GluN1-NMDAR (red) after 1 h exposure to buffer, D-AP5 (50 μM), KET (1 μM), or MK-801 (20 μM). Scale bar, 5 μm.

(B) Synaptic NMDAR cluster area (left) and intensity (right) after exposure to buffer (n = 50 cells), D-AP5 (n = 40), KET (n = 36), MK-801 (n = 31), or TTX (n = 41). Data expressed as median ± 25%–75% IQR (box) and min to max (whiskers). Each dot represents the mean synaptic NMDAR cluster area (left) and intensity (right) for one cell, respectively.

peptides mimicking the C-terminal sequences of GluN2B-NMDAR subunits to interfere with the binding of NMDAR to PDZ domains[8,35] prevented the ability of KET to increase FRET efficiency between GluN1-GFP and GluN1-mCherry within NMDAR clusters (Figures 4A–4C; Figures S6A–S6C), suggesting that this mechanism requires a physical interplay with MAGUKs.

We further investigated the contribution of MAGUKs to drug-induced NMDAR synaptic trapping by quantifying FLIM-FRET between GluN1-GFP and mCherry-labeled PSD-95, a prototypical example of PDZ-domain-containing protein providing a major contribution to NMDAR anchoring at the PSD[35] (Figure 4D). As previously reported,[32] acute exposure to NMDA decreased FRET efficiency in dendritic spine clusters co-expressing GluN1-GFP and PSD-95-mCherry, reflecting a dissociation of NMDAR/PSD-95 complexes upon receptor activation (Figures 4E and 4F; Figure S6D). Although this decrease persisted in the presence of MEM and was partially restrained by D-AP5, co-application with KET and MK-801 prevented the action of NMDA, indicating that the binding of these drugs avoided dissociation and favored the persistence of NMDAR/PSD-95 complexes (Figures 4E and 4F; Figures S6D and S6E). Finally, we probed the role of these interactions in drug-elicited NMDAR synaptic trapping using SPT to track wild-type (WT) or recombinant FLAG-tagged GluN2A- and GluN2B-NMDARs (Figures 4G and 4H). Although acute co-exposure to NMDA and KET in the presence of TTX enhanced the confinement and increased the residency time of WT receptors at excitatory synapses, introducing a single point mutation in GluN2A (S1462A) and GluN2B (S1480A) cytosolic domains to prevent the binding to PDZ-domain-containing scaffolds occluded the action of the drug (Figures 4G and 4H). Together, these findings indicate that KET and MK-801 enhance the synaptic trapping of NMDAR by driving conformational rearrangements in cytosolic receptor domains that strengthen interactions with PDZ domain scaffolding proteins.

KET prevents impairments in NMDAR synaptic anchoring and signaling caused by patient-derived anti-NMDAR antibodies

Deciphering the molecular mechanisms underlying the multiple therapeutic properties of KET is a major challenge. Building on our results, we wondered whether some of these properties might result from its ability to trap NMDAR at synapses. To address this question, we took advantage of our understanding of anti-NMDAR encephalitis, a severe brain condition in which NMDAR-IgG directed against NMDAR extracellular domains cause psychotic-like manifestations and life-threatening neurological dysfunctions.[36] From a mechanistic point of view,

NMDAR-IgG do not compromise NMDAR channel properties but disrupt protein-protein interactions between NMDAR and transmembrane partners, thereby triggering a dispersal of synaptic receptors and a hypofunction of NMDAR-mediated transmission and plasticity.[13,15,17] Thus, we explored whether synaptic anchoring promoted by KET could counteract the pathological destabilization of synaptic NMDARs caused by patient-derived NMDAR-IgG, using a higher drug concentration (10 μM) that ensured rapid and efficient targeting of a large fraction of receptors.

Using SPT, we first confirmed that exposure to purified NMDAR-IgG or cerebrospinal fluid (CSF) from patients with anti-NMDAR encephalitis impaired receptor trapping at excitatory synapses (Figures 5A–5D; Figures S7A–S7C).[17] Strikingly, co-application of KET—but not D-AP5—prevented the destabilizing action of NMDAR-IgG and favored NMDAR synaptic anchoring (Figures 5A–5D; Figures S7B–S7D). Ensemble imaging of super-ecliptic pHluorin (SEP)-tagged GluN2A-NMDAR populations through fluorescence recovery after photobleaching (FRAP) further confirmed these observations and showed that while NMDAR-IgG increased the fraction of mobile receptors at synapses, exposing neurons to KET averted this deleterious action (Figures 5D and 5E). It is noteworthy that the benzodiazepine midazolam currently used as a sedative treatment for patients with anti-NMDAR encephalitis did not replicate the compensatory action of KET, advocating for a selective operation on NMDAR (Figure S7D). This reversal likely involved drug-induced cytosolic rearrangements in the C-terminal domains of the receptors, as depicted above (Figure 3), because FLIM-FRET monitoring from GluN1-GFP/GluN1-mCherry-incorporating NMDAR complexes showed that exposure to NMDAR-IgG caused an increase in the lifetime of GFP fluorescence within dendritic spine receptor clusters that was abolished by co-exposure with KET but persisted upon co-exposure with D-AP5 (Figures 5F–5H; Figure S7E). At the macromolecular level, KET—unlike D-AP5—administration compensated for NMDAR-IgG-elicited impairments in the number of NMDAR-containing synapses and in the abundance of receptors within synaptic clusters without affecting the density of synapses or the properties of PSD scaffolding protein clusters (Figures 6A and 6B; Figures S8A–S8C). Altogether, these results demonstrate that enhanced synaptic trapping elicited by KET counterbalances the pathological destabilization of NMDARs caused by NMDAR-IgG.

NMDAR-IgG-induced removal of synaptic receptors results in severe hypofunction of NMDAR-mediated signaling.[37] To explore whether the stabilizing action of KET could prevent such impairments, we monitored the activity of CaMKIIα, one

(C) Left, experimental principle. Middle, dendritic segment with Homer1c-GFP (upper left) and FLAG-GluN1 (upper right), and tessellated, super-resolved image of FLAG-GluN1 detections in direct stochastic optical reconstruction microscopy (dSTORM) (lower). Scale bars, 5 μm (upper) and 2 μm (lower). Right, a tessellated, super-resolved GluN1-NMDAR cluster after exposure to buffer. Each dot represents a detection and thick outlines indicate intra-cluster nanodomains of receptors. Scale bars, 100 nm.

(D) Tessellated, super-resolved GluN1-NMDAR clusters after exposure to D-AP5, KET, MK-801, or TTX. Scale bar, 100 nm.

(E) Upper, area (left) and density (right) of GluN1-NMDAR clusters after exposure to buffer (n = 181 clusters), D-AP5 (n = 79), KET (n = 179), MK-801 (n = 113), or TTX (n = 139). Lower, area (left) and density (right) of GluN1-NMDAR nanodomains after exposure to buffer (n = 561 nanodomains), D-AP5 (n = 222), KET (n = 522), MK-801 (n = 327), or TTX (n = 330). Data expressed as median ± 25%–75% IQR (box) and 10%–90% percentile (whiskers). Kruskal-Wallis followed by Dunn's multiple comparison test, ***p < 0.001.

See also Figure S4 for additional experiments related to Figure 2.
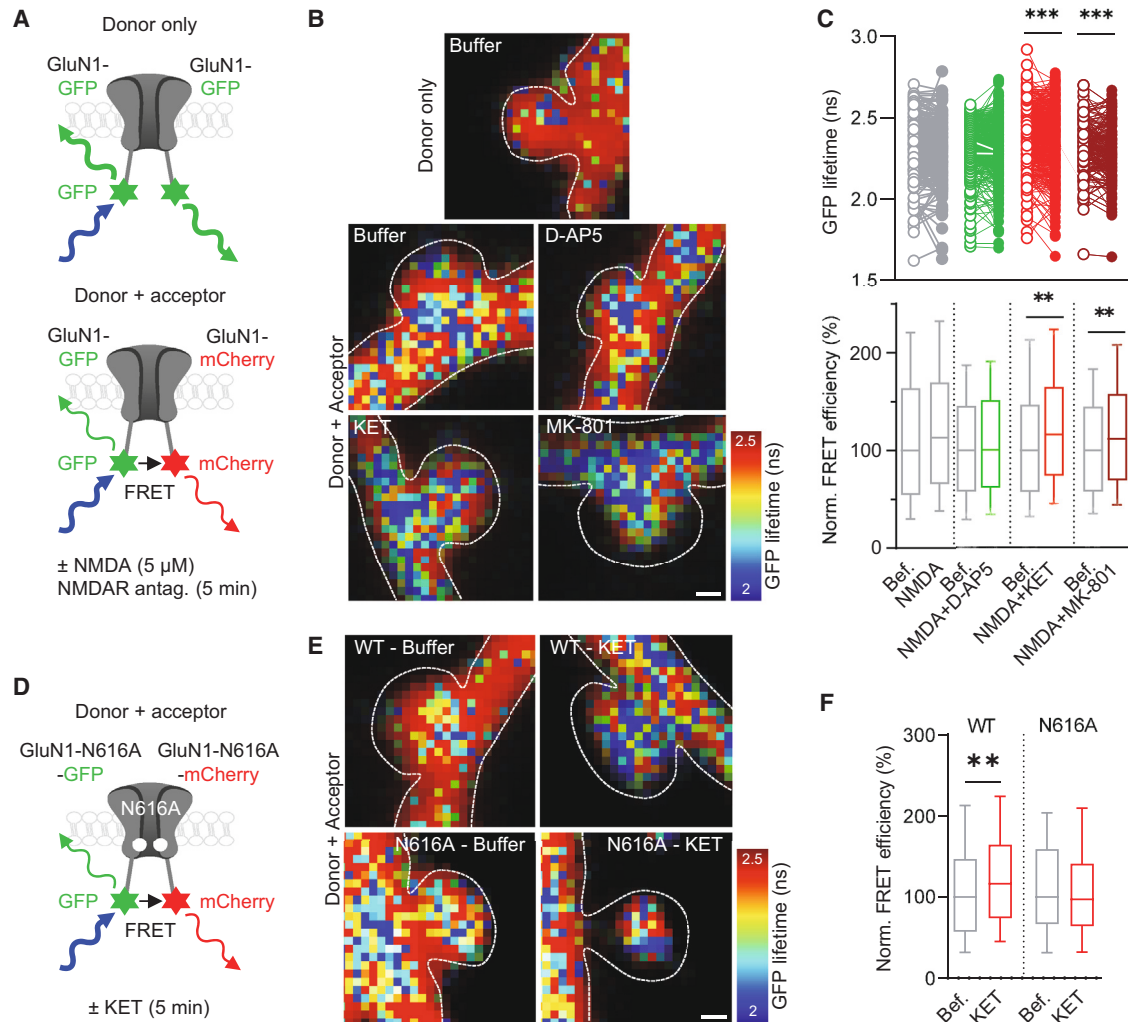
Figure 3. KET drives conformational changes in NMDAR cytosolic domains

(A) Principle of intramolecular FLIM-FRET experiments.

(B) GFP lifetime in GluN1-GFP (donor only) and GluN1-GFP/GluN1-mCherry (donor + acceptor) dendritic spine clusters after exposure to buffer or NMDA (5 μM) combined with D-AP5 (50 μM), KET (1 μM), or MK-801 (20 μM). Scale bar, 1 μm.

(C) Upper, GFP lifetime in GluN1-GFP/GluN1-mCherry clusters before and after exposure to NMDA combined with D-AP5 (n = 373 clusters), KET (n = 498), or MK-801 (n = 239). Each dot represents the lifetime of one cluster, before and after treatment. Wilcoxon test, ***$p < 0.0001$. Lower, FRET efficiency in GluN1-GFP/GluN1-mCherry clusters before and after exposure to NMDA combined with D-AP5 (n = 385 clusters), KET (n = 326), or MK-801 (n = 239). Data expressed as median ± 25%–75% IQR (box) and 10%–90% percentile (whiskers). Mann-Whitney test, **$p < 0.01$.

(D) GluN1-GFP/GluN1-mCherry FRET couple incorporating the N616A point mutation.

(E) GFP lifetime in GluN1-GFP/GluN1-mCherry (WT) or GluN1-N616A-GFP/GluN1-N616A-mCherry (N616A) dendritic spine clusters after exposure to buffer or NMDA combined with KET. Scale bar, 1 μm.

(F) FRET efficiency in GluN1-GFP/GluN1-mCherry (WT, n = 326 clusters) and GluN1-N616A-GFP/GluN1-N616A-mCherry (N616A, n = 362) clusters before and after exposure to NMDA combined with KET. Data expressed as median ± 25%–75% IQR (box) and 10%–90% percentile (whiskers). Mann-Whitney test, **$p < 0.01$.

See also Figure S5 for additional experiments related to Figure 3.

of the main downstream effectors associated with NMDAR and a central initiator of synaptic plasticity. Using the FRET-based sensor Green-Camuiα,[38] we measured intramolecular FLIM-FRET as a proxy for kinase activity (Figure 6C). Exposure to NMDAR-IgG significantly reduced the amplitude of glutamate-elicited (25 μM, 2 min) increase in monomeric enhanced GFP (mEGFP) fluorescence lifetime, consistent with an autoanti-

body-induced hypofunction of NMDAR and CaMKIIα (Figures 6D and 6E). Remarkably, co-application of KET counteracted the impact of NMDAR-IgG and restored CaMKIIα activity to baseline levels, while KET alone at this concentration had no impact and co-application of D-AP5 worsened impairments in CaMKIIα activity (Figures 6D and 6E). Thus, enhanced synaptic trapping promoted by KET mitigates impairments in NMDAR

Neuron
Article
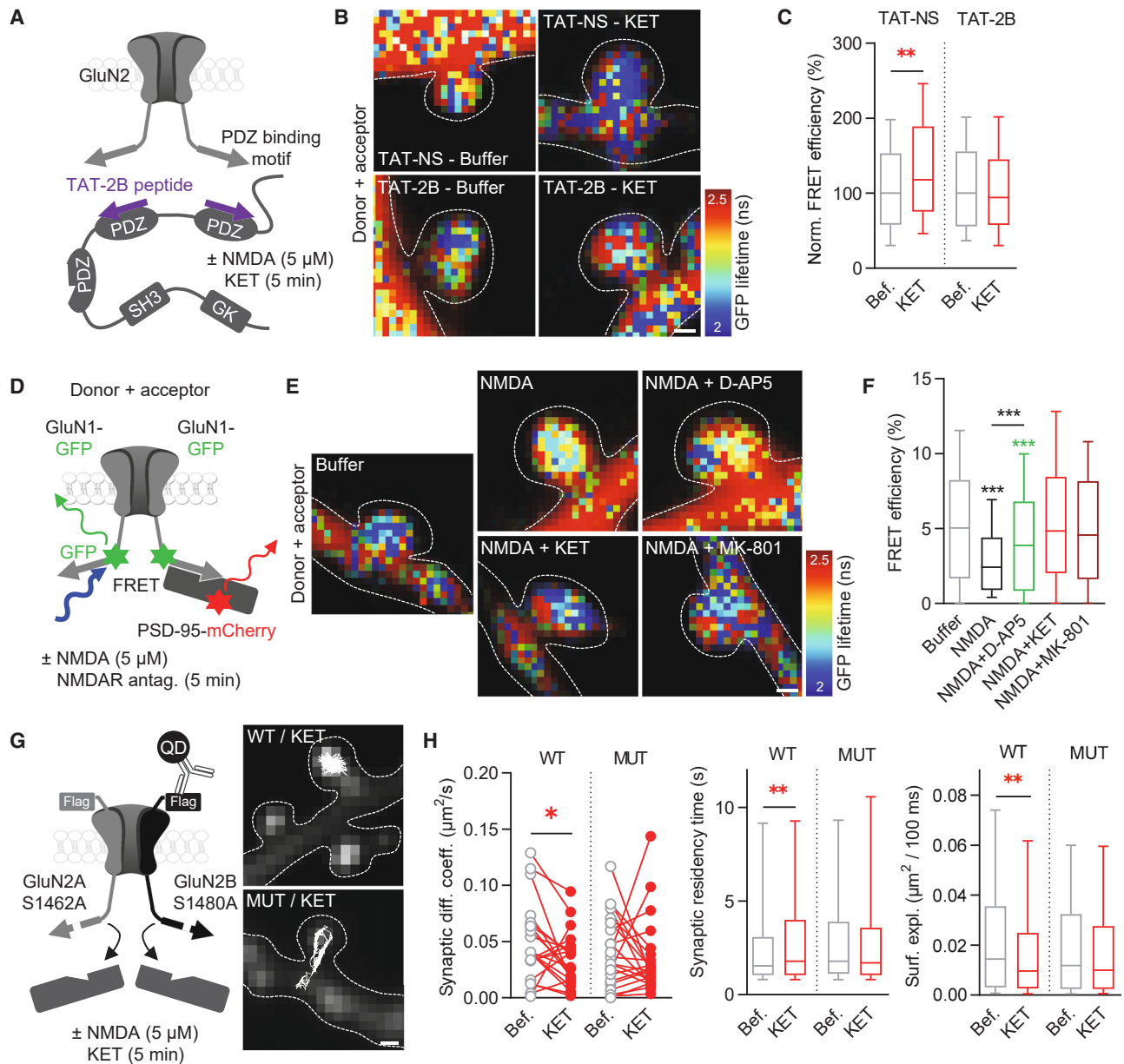
Figure 4. KET favors synaptic trapping through enhanced interaction with PDZ-domain-containing scaffolding proteins

(A) Action of TAT-2B competing peptides.

(B) GFP lifetime in GluN1-GFP/GluN1-mCherry dendritic spine clusters before and after NMDA combined with KET in the presence of TAT-NS or TAT-2B peptides (10 μM). Scale bar, 1 μm.

(C) FRET efficiency in GluN1-GFP/GluN1-mCherry clusters before and NMDA combined with KET in the presence of scramble TAT-NS (n = 205 clusters) or TAT-2B (n = 243). Data expressed as median ± 25%–75% IQR (box) and 10%–90% percentile (whiskers). Mann-Whitney test, **p < 0.01.

(D) Inter-molecular FLIM-FRET experiments.

(E) GFP lifetime in GluN1-GFP/PSD-95-mCherry dendritic spine clusters after exposure to buffer or NMDA alone combined with D-AP5, KET, or MK-801. Scale bar, 1 μm.

(F) FRET efficiency in GluN1-GFP/PSD-95-mCherry clusters after exposure to buffer (n = 895 clusters) or NMDA (n = 761) alone or combined with D-AP5 (n = 723), KET (n = 535), or MK-801 (n = 606). Data expressed as median ± 25%–75% IQR (box) and 10%–90% percentile (whiskers). Kruskal-Wallis followed by Dunn's multiple comparison test, ***p < 0.001.

(G) Dendritic segments expressing Homer1c-dsRed (gray) with representative trajectories of QD-labeled WT FLAG-GluN2A/FLAG-GluN2B and mutated FLAG-GluN2A-S1462A/FLAG-GluN2B-S1480A synaptic NMDAR exposed to NMDA combined with KET. Scale bar, 500 nm.

(H) Left, instantaneous diffusion coefficients of wild-type FLAG-GluN2A/FLAG-GluN2B (WT, n = 21 cells) and FLAG-2A-S1462A/FLAG-2B-S1480A (MUT, n = 22) synaptic NMDAR before and after NMDA and KET in the presence of TTX. Each dot represents the median diffusion coefficient for one cell, before and after treatment. Paired t test, *p < 0.05. Middle, synaptic residency time of WT (n = 21) and MUT (n = 22) synaptic NMDAR before (WT, n = 548 trajectories; MUT,

(legend continued on next page)

synaptic anchoring and signaling elicited by encephalitis patient NMDAR-IgG.

KET alleviates anxiety- and sensorimotor-gating-related behavioral deficits caused by patient antibodies

Building on the ability of KET to compensate for the synaptic impairments occurring upon exposure to NMDAR-IgG *in vitro*, we finally assessed whether KET also displayed the ability to improve behavioral deficits caused by patient NMDAR-IgG. We developed a rat model based on a 14-day continuous delivery of NMDAR-IgG into the CSF through the subcutaneous implantation of an osmotic pump connected to a cannula unilaterally implanted in a cerebral ventricle (Figure 7A).[39] After surgery, rats were allowed to recover for a period of 10 days before undertaking a battery of behavioral assays in order to characterize potential manifestations of anhedonia (sucrose consumption), anxiety (elevated plus maze), despair (forced swim test), or evidence of locomotion (open field), memory (novel object recognition), or sensorimotor gating (prepulse inhibition) deficits (Figure 7A). Comparison with saline-exposed animals (sham) showed that infusing IgG from healthy individuals (Healthy-IgG), alone or combined with KET, did not affect behavioral performances in any of the tests (Figure S9). Likewise, infusing Healthy-IgG, NMDAR-IgG alone or combined with KET or 3-(2-Carboxypiperazin-4-yl)propyl-1-phosphonic acid (CPP, an analog of D-AP5) did not substantially impact locomotor activity, as illustrated by Z scores calculated on the basis of horizontal activity and velocity in the open field test (Figures 7B–7E), and none of the experimental conditions affected memory performances in the novel object recognition test either (Figure 7L).

Assessing behavioral features related to anxiety and depression, we observed that the time spent in open arms of the elevated plus maze and in the center zone of the open field were not affected by NMDAR-IgG, infused alone or together with KET or CPP (Figures 7F–7H). However, rats infused with NMDAR-IgG displayed lower sucrose consumption compared with those exposed to Healthy-IgG. Strikingly, sucrose consumption in NMDAR-IgG + KET-treated and Healthy-IgG-treated rats was not different when NMDAR-IgG + CPP-treated and NMDAR-IgG-treated animals were undistinguishable, suggesting that patient NMDAR-IgG trigger manifestations of anhedonia that are compensated by KET (Figure 7I). Consistently, rats exposed to NMDAR-IgG were more immobile in the forced swim test, and this feature was alleviated both by KET and CPP (Figure 7J). Most importantly, we combined all data from sucrose consumption, forced swim, open field, and elevated plus maze tests to yield a Z score for each condition (Figure 7K). The Z score value was significantly lower in animals exposed to NMDAR-IgG when compared with the Healthy-IgG condition, indicating that patient NMDAR-IgG favor the development of behavioral features of anxiety and depression. The NMDAR-Ig effect was fully reversed by KET, whereas NMDAR-Ig and NMDAR-Ig + CPP

score values were statistically not different (Figure 7K). In addition, rats infused with NMDAR-IgG or NMDAR-IgG + CPP responded poorly to the prepulse inhibition test when compared with animals receiving Healthy-IgG or NMDAR-IgG + KET, indicative of sensorimotor gating deficits triggered by patient NMDAR-IgG that were improved by KET (Figure 7M). Collectively, these data indicate that KET alleviates anxiety- and sensorimotor-gating-related behavioral deficits provoked by patient NMDAR-IgG.

DISCUSSION

NMDAR are targeted by several therapeutic drugs used daily in clinics, ranging from general anesthetics (e.g., KET) to cognitive enhancers prescribed for the treatment of Alzheimer's disease (e.g., MEM).[2] Unfortunately, our understanding of their action mode is fragmented, and deciphering whether the sedative, psychotomimetic, or antidepressant properties of clinically relevant NMDAR modulators originate from identical or distinct molecular mechanisms remains challenging. The recent repurposing of KET as an antidepressant has put the spotlight on NMDAR antagonism as a strategy for the treatment of mental illnesses. However, most attempts so far to identify better-tolerated drugs sharing the beneficial properties of KET and devoid of its adverse effects have yielded disappointing outcomes, suggesting that the psychoactive actions of NMDAR antagonists do not result exclusively from modulations of channel gating and involve additional features. Recent advances in the structural biology of NMDAR provided insightful information on the binding mechanisms and conformational rearrangements of extracellular and transmembrane domains caused by OCBs.[33,40] However, the labile nature of cytosolic domains makes them less amenable to structural studies and still limits our understanding of how drug-elicited conformational rearrangements may translate into modulations of interactions with cytosolic proteins. Our comparative exploration of the impact of competitive (D-AP5), uncompetitive (KET, MK-801, and MEM), and glycine site (KA) antagonists provides evidence that while all drugs efficiently block NMDAR-mediated ion fluxes, changes in the conformation of cytosolic domains selectively elicited by short-term exposures to OCBs promote interactions with PDZ-domain-containing scaffolds and thereby enhance receptor trapping at synapses. Thus, the action of OCBs may encompass an unsuspected mosaic of ionotropic- and non-ionotropic processes.

How could the trapping of ionotropically silenced NMDAR by OCBs be of any benefit to synaptic function? Activity-dependent adjustments in NMDAR synaptic trapping and organization emerge as powerful mechanisms, allowing rapid adaptations of NMDAR signaling without necessary changes in synaptic receptor numbers.[4,29] Surface-diffusion-based rearrangements in NMDAR localization play a major structural role in NMDAR-mediated CaMKII signaling, as the physical interaction between

---

Neuron
Article

CellPress
OPEN ACCESS
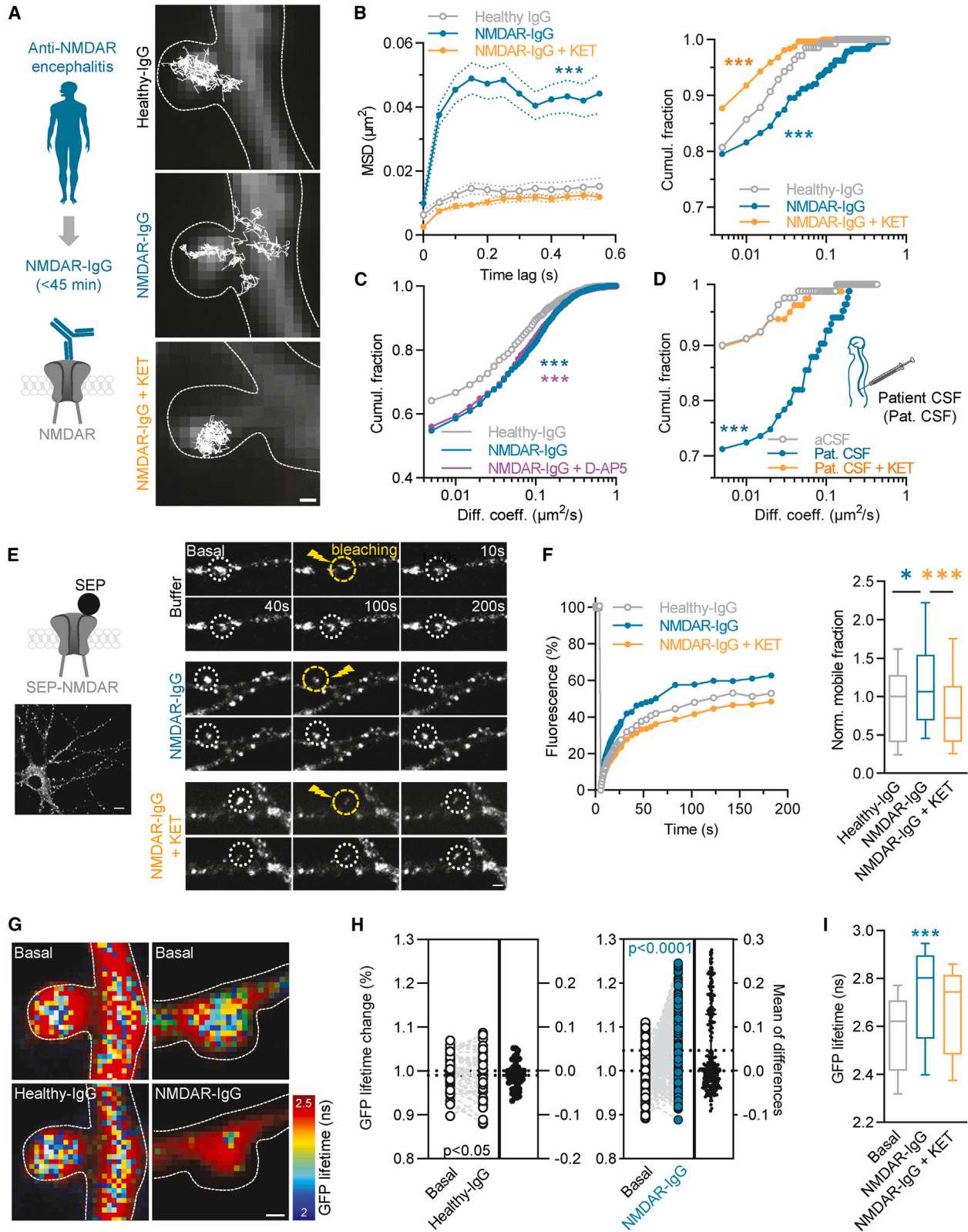
receptors and the kinase allows its translocation and stabilization to dendritic spines, a molecular mechanism that shapes the plastic fate of synapses and allows memory formation and persistence.[41] Reciprocally, interactions with CaMKII shape the organization of NMDAR synaptic clusters, and destructuring receptor nanodomains has profound consequences on synaptic plasticity, suggesting that the nanoscale organization of CaMKII/NMDAR complexes contributes to the spatiotemporal orchestration of biochemical reactions supporting synaptic signaling.[8,42,43] Here, we show that low doses of KET do not silence basal CaMKIIα synaptic activity but instead prevent its impairment caused by NMDAR-IgG, indicating that OCBs preserve glutamate-driven NMDAR signaling despite precluding NMDAR-mediated calcium influx. It further suggests that by maintaining the pool and nanoscale architecture of NMDAR synaptic complexes, OCBs could stabilize NMDAR signaling at synapses that are exposed to damaging stimuli. Interestingly, the ability of OCBs to favor the synaptic anchoring of membrane proteins may extend beyond NMDAR. Indeed, KET was recently reported to bind the tropomyosin receptor kinase B (TrkB), i.e., the receptor of brain-derived neurotrophic factor (BDNF), and to favor its synaptic stabilization and signaling. This allosteric facilitation of BDNF signaling involves the binding of KET to a cholesterol-sensitive domain within the receptor transmembrane segment and the formation of receptor multimers.[44] Because KET also rapidly redistributes cholesterol within the plasma membrane[45] and can modulate NMDAR via a hydrophobic membrane path through a gated fenestration,[46] it is plausible that KET may alter NMDAR intracellular domain conformation and synaptic trapping through cholesterol/lipid-mediated mechanisms. Though, the fact that KET did not affect the synaptic trapping and organization of $K_V1.3$, EphB2R, or $GABA_AR$ indicates that its action is selective and not a mere change in membrane properties that would affect all membrane proteins indistinctively.

Over the past decades, substantial progress has been made in dissecting how impairments in NMDAR function may participate in the onset of brain diseases. However, endeavors aiming at rescuing these dysfunctions through pharmacological interventions on NMDAR channel gating have repeatedly failed, either because of limited efficacy or as a result of damaging adverse effects, urging the need for alternative therapeutic approaches. Accumulating evidence from pre-clinical animal models suggests that abnormalities affecting channel-unrelated features of NMDAR function may contribute to the etiology of mental and neurological illnesses. Convincing illustrations include the participation of non-ionotropic NMDAR-mediated signaling mechanisms in glutamate-elicited excitotoxicity,[47–50] the implications of aberrant NMDAR redistributions at the surface of striatal neurons in l-3,4-dihydroxyphenylalanine (L-DOPA)-induced dyskinesia and Huntington's disease,[51,52] or the description of Aβ-initiated disruption of NMDAR synaptic anchoring[53,54] and non-ionotropic NMDAR-mediated synaptic depression and dendritic spine loss in Alzheimer's disease.[55–58]

The discovery of neuropsychiatric conditions, such as anti-NMDAR encephalitis, in which NMDAR-IgG cause a severe hypofunction of NMDAR-mediated signaling that gives rise to a combination of psychiatric and neurological manifestations without altering channel gating,[19,36,59] further fed this new field of investigation. Raising the expression of transmembrane and/or cytosolic scaffolds (i.e., EphB2R and PSD-95) or administering ligands (e.g., ephrin B2) to promote the stabilization of NMDAR have been proposed as therapeutic options to alleviate the synaptic and cognitive deficits associated with the Alzheimer's disease and anti-NMDAR encephalitis, respectively.[53,56,60] Additionally, recent studies in genetic-, developmental-, and immune-based models of psychosis suggest that manipulating NMDAR synaptic redistributions could represent a powerful strategy to counterbalance molecular deficits associated with mental disorders.[61,62] Here, we show that enhanced

Figure 5. KET prevents impairments in NMDAR synaptic trapping and conformational rearrangements caused by patient-derived anti-NMDAR antibodies

(A) Left, patients' IgG purification. Right, dendritic segments expressing Homer1c-dsRed with representative trajectories of QD-labeled GluN2A-NMDAR after 30 min exposure to Healthy-IgG (upper), NMDAR-IgG (middle), or NMDAR-IgG + KET (10 μM; lower). Scale bar, 500 nm.

(B) MSD (left) and cumulative distributions of instantaneous diffusion coefficients (right) of synaptic NMDAR after exposure to Healthy-IgG (n = 140 trajectories), NMDAR-IgG (n = 240), or NMDAR-IgG + KET (n = 318). Kolmogorov-Smirnov test, ***p < 0.0001.

(C) Cumulative distributions of instantaneous diffusion coefficients of synaptic NMDAR after exposure to Healthy-IgG (n = 1,578 trajectories), NMDAR-IgG (n = 1,794), or NMDAR-IgG + D-AP5 (50 μM; n = 1,881). Kolmogorov-Smirnov test, ***p < 0.0001.

(D) Left, CSF sampling (spinal tap) from a patient suffering from anti-NMDAR encephalitis. Right, cumulative distributions of instantaneous diffusion coefficients of synaptic NMDAR after artificial CSF (aCSF, n = 63 trajectories), patient CSF (n = 54), or Pat. CSF + KET (n = 55). Kolmogorov-Smirnov test; ***p < 0.001.

(E) Left, schematic representation of a SEP-tagged NMDAR and representative neuron expressing SEP-GluN2A-NMDAR. Scale bars, 10 μm. Right, dendritic segments illustrating recovery from photobleaching in SEP-GluN2A-NMDAR clusters (white dotted circles) after 20 min exposure to buffer, NMDAR-IgG, or NMDAR-IgG + KET. Scale bars, 2 μm.

(F) Left, fluorescence recovery after photobleaching in SEP-GluN2A-NMDAR clusters. Each curve represents the mean of regions of interest for a representative neuron. Right, mobile fraction of SEP-GluN2A-NMDAR after exposure to Healthy-IgG (n = 234 region of interest [ROI]), NMDAR-IgG (n = 332), or NMDAR-IgG + KET (n = 262). Data expressed as median ± 25%–75% IQR (box) and 10%–90% percentile (whiskers). One-way ANOVA followed by Tukey's multiple comparison test, *p < 0.05, ***p < 0.001.

(G) GFP lifetime in GluN1-GFP/GluN1-mCherry dendritic spine clusters in basal condition and 15 min after exposure to Healthy-IgG or NMDAR-IgG. Scale bar, 1 μm.

(H) GFP lifetime in GluN1-GFP/GluN1-mCherry clusters before and 15 min after exposure to Healthy-IgG (n = 50 ROI) or NMDAR-IgG (n = 174). Each dot represents the median lifetime for one cell, before and after treatment. Unpaired t test ***p < 0.001.

(I) GFP lifetime in GluN1-GFP/GluN1-mCherry clusters, before and after NMDAR-IgG alone then NMDAR-IgG + KET (n = 417 clusters). Data expressed as median ± 25%–75% IQR (box) and 10%–90% percentile (whiskers). Paired t test ***p < 0.001.

See also Figure S7 for additional experiments related to Figure 5.

Neuron
Article
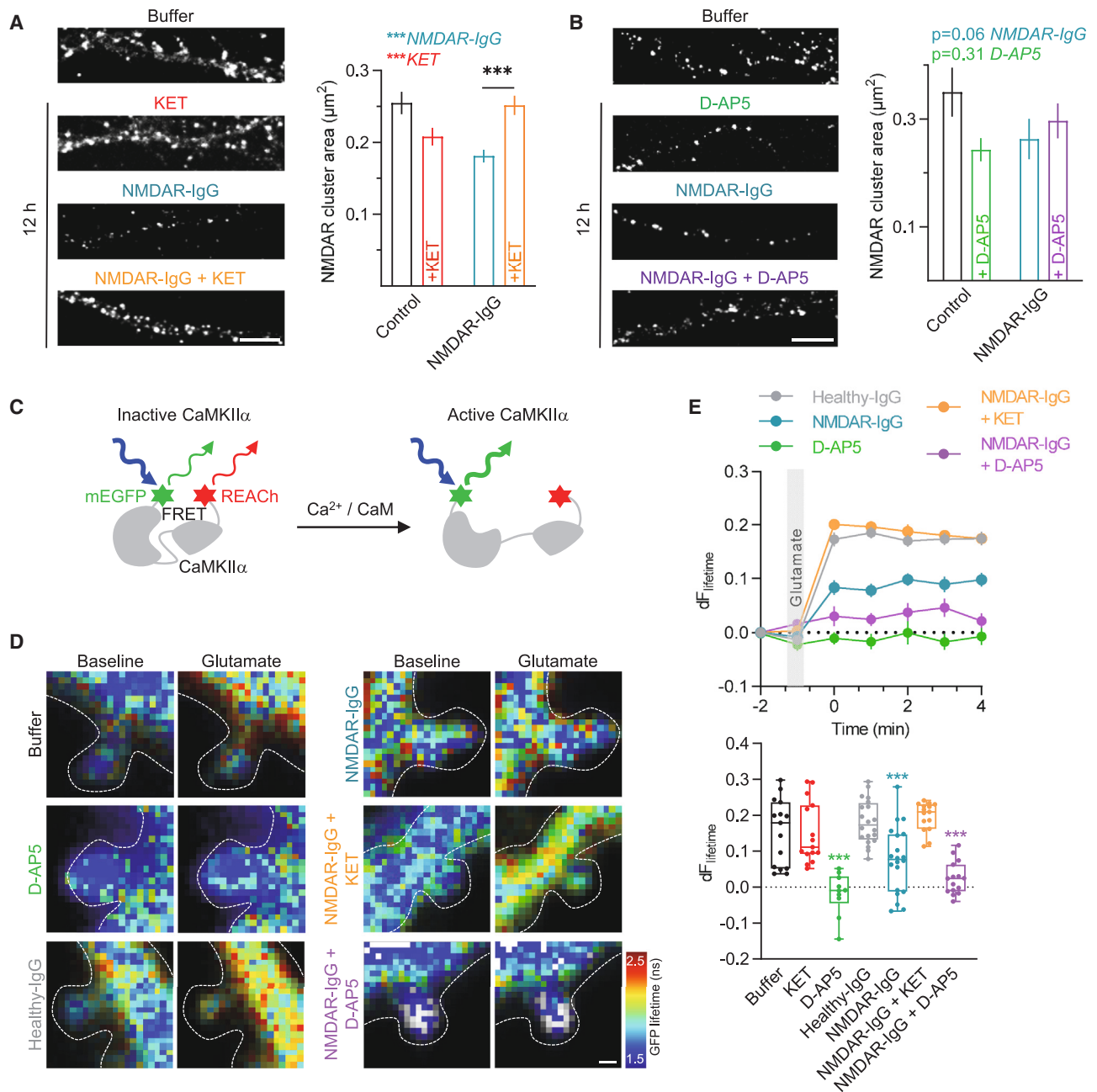
Figure 6. KET prevents synaptic NMDAR depletion and signaling deficits caused by patient-derived anti-NMDAR antibodies

(A) Left, dendritic segments immunostained for surface GluN2B-NMDAR after buffer, KET, NMDAR-IgG, or NMDAR-IgG + KET. Scale bar, 2 µm. Right, synaptic NMDAR cluster area after buffer ($n = 184$ clusters), KET ($n = 103$), NMDAR-IgG ($n = 221$), NMDAR-IgG + KET ($n = 219$). Data expressed as mean ± SD. Two-way ANOVA followed by Tukey's multiple comparison test, ***$p < 0.001$.

(B) Left, dendritic segments immunostained for surface GluN2B-NMDAR after exposure to buffer, D-AP5, NMDAR-IgG, or NMDAR-IgG + D-AP5. Scale bar, 2 µm. Right, synaptic NMDAR cluster area after buffer ($n = 78$ clusters), D-AP5 ($n = 88$), NMDAR-IgG ($n = 64$), NMDAR-IgG + D-AP5 ($n = 93$). Data expressed as mean ± SD.

(C) Principle of intramolecular FLIM-FRET experiments.

(D) GFP lifetime in Green-Camuiα dendritic spine clusters before and after glutamate (25 µM) in the presence of buffer, D-AP5 (50 µM), Healthy-IgG, NMDAR-IgG, NMDAR-IgG + KET, or NMDAR-IgG + D-AP5. Scale bar, 1 µm.

(E) Time lapse (upper) and quantifications (time point 2 min; lower) of GFP lifetime in Green-Camuiα dendritic spine clusters before and after glutamate in the presence of buffer ($n = 15$ clusters), KET (10 µM; $n = 15$), D-AP5 (50 µM; $n = 13$), Healthy-IgG ($n = 35$), NMDAR-IgG ($n = 35$), NMDAR-IgG + KET ($n = 15$), or NMDAR-IgG + D-AP5 ($n = 15$). Data expressed as median ± 25%–75% IQR (box) and 10%–90% percentile (whiskers). Each dot represents the lifetime for one cluster. One-way ANOVA followed by Tukey's multiple comparison test, ***$p < 0.001$.

See also Figure S8 for additional experiments related to Figure 6.

(legend on next page)

CellPress
OPEN ACCESS

Neuron
Article
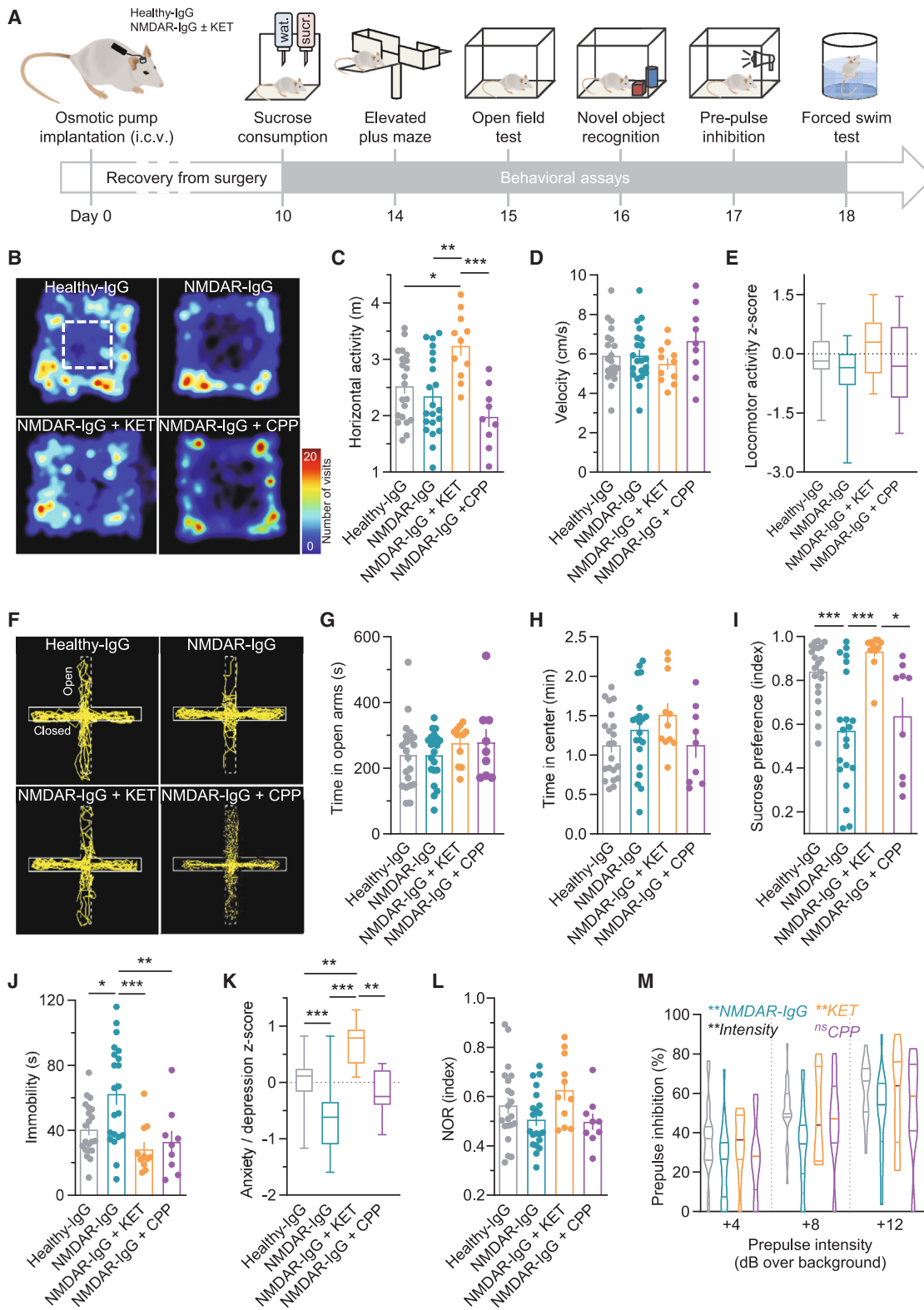
NMDAR synaptic trapping triggered by KET compensates for depletion in synaptic receptors and corrects signaling and behavioral deficits caused by NMDAR-IgG from patients with anti-NMDAR encephalitis. KET appears particularly efficient at alleviating behavioral features of anxiety and depression, as well as sensorimotor gating deficits provoked by NMDAR-IgG. Although using an antagonist to compensate for symptoms resulting from NMDAR hypofunction may sound counterintuitive, two decades of investigations have revealed that the antidepressant action of KET paradoxically relies on a wave of neural plasticity in the corticomesolimbic circuitry supporting reward and mood.[63,64] These mechanisms involve either NMDAR inhibition on principal cells or interneurons, causing release of BDNF, or direct binding of the drug to TrkB, all of which elicit TrkB activation and mammalian target of rapamycin (mTOR) signaling, allowing protein synthesis and synaptic adaptation.[65] Remarkably, enhanced synaptic trapping of plasticity-related receptors emerges as a common feature of several antidepressants, as the direct binding of KET and fluoxetine to TrkB, or the actions of tianeptine and KET on AMPA glutamate receptors, were both reported to promote interactions with PDZ-domain-containing scaffolds and to extend the transient anchoring of these receptors at excitatory connections.[44,66–69] Thus, targeting the synaptic trapping of neurotransmitter and neurotrophin receptors appears as a promising research track to compensate for molecular impairments associated with psychiatric illnesses. Although the molecules described to promote receptor anchoring so far exhibit a polypharmacological profile limiting their clinical use, developing compounds acting on synaptic trapping exclusively without harming other receptor functions or secondary targets could provide innovative therapeutic strategies for the treatment of brain disorders involving glutamatergic dysfunction.

Limitations of the study

Here, we characterized OCB-elicited changes in conformation, interactions, synaptic trapping, and nanoscale organization of all NMDARs without subtype-based distinction. Given the variety of composition and subsequent functions of these receptors,

and considering recent reports suggesting that psychotomimetic and antidepressant properties of OCBs might result from subtype-selective targeting,[70] exploring whether OCBs preferentially affect the synaptic trapping and organization of NMDAR incorporating specific sets of GluN2 and/or GluN3 subunits will be of major interest. Furthermore, while we limited our investigations to hippocampal pyramidal cells, repeated reports of dysfunctions affecting NMDAR expressed by interneurons in neuropsychiatric disorders, and a growing body of evidence proposing them as preferential targets supporting the psychoactive properties of KET, call for similar investigations on other cell types. Exploring whether specific brain areas may be more prone to OCB action will also be important step, as recent reports indicate that the antidepressant action of KET specifically involves a use-dependent trapping of KET in NMDAR in the lateral habenula.[71,72] Finally, whether magnesium—i.e., the physiological NMDAR pore blocker—shares similar properties as OCBs and acts as an endogenous regulator controlling not only channel gating but also NMDAR synaptic trapping to ensure receptor activation at right time and location is an exciting question that will need to be addressed.

STAR★METHODS

Detailed methods are provided in the online version of this paper and include the following:

- KEY RESOURCES TABLE
- RESOURCE AVAILABILITY
  - Lead contact
  - Materials availability
  - Data and code availability
- EXPERIMENTAL MODEL AND SUBJECT DETAILS
  - Human samples
  - Animal experiments
  - Primary hippocampal cell cultures
- METHOD DETAILS
  - Cerebroventricular infusions
  - Behaviour experiments
  - Z-score calculations
  - Transfection
  - Immunostaining

Figure 7. KET reverses anxiety- and sensorimotor-gating-related behavioral deficits caused by patient antibodies
(A) Timeline of behavior experiments of rats infused with saline (Sham; n = 15 rats), IgG from healthy individuals alone (Healthy-IgG, n = 21) or combined with KET (Healthy-IgG + KET, n = 9), patient IgG (NMDAR-IgG, n = 21) alone or combined with either KET (NMDAR-IgG + KET, n = 11) or CPP (NMDAR-IgG + CPP; n = 9) over 14 days.
(B) Heatmaps of the visits in central or wall zones of the open field arena of animals exposed to either Healthy-IgG, NMDAR-IgG alone, or combined with KET.
(C–E) Horizontal activity (C), velocity (D), and Z scores for locomotor activity (E) calculated from horizontal activity and velocity measurements of animals exposed to either Healthy-IgG or NMDAR-IgG alone or combined with either KET or CPP. All data expressed as scatter dot plot with mean ± SEM, except for (E) displayed as median ± 25%–75% IQR (box) and 10%–90% percentile (whiskers). One-way ANOVA followed by Tukey's multiple comparisons test, *p < 0.05, **p < 0.01, ***p < 0.001.
(F) Tracks (yellow) in the open and closed arms of the elevated plus maze of animals exposed to either Healthy-IgG or NMDAR-IgG alone or combined with KET.
(G–K) Time within open arms (G, elevated plus maze), time in center zone (H, open field test), sucrose preference index (I, sucrose consumption), time spent immobile (J, forced swim test), and Z scores for anxiety/depression calculated from sucrose consumption, forced swim, open field, and elevated plus maze tests of animals exposed to either Healthy-IgG or NMDAR-IgG alone or combined with either KET or CPP. All data expressed as scatter dot plot with mean ± SEM except for (K) displayed as median ± 25%–75% IQR (box) and 10%–90% percentile (whiskers). One-way ANOVA followed by Tukey's multiple comparisons test, *p < 0.05, **p < 0.01, ***p < 0.001.
(L) Novel object recognition (NOR) index of animals exposed to either Healthy-IgG or NMDAR-IgG alone or combined with KET or CPP.
(M) PPI of startle responses of animals exposed to either Healthy-IgG or NMDAR-IgG alone or combined with KET or CPP for prepulse intensities of +4 dB, +8 dB, and +12 dB over background. All data expressed as violin plot with median ± 25%–75% IQR lines. Two-way ANOVA followed by Tukey's multiple comparisons test, **p < 0.01.
See also Figure S9 for additional experiments related to Figure 7.

Neuron
Article

CellPress
OPEN ACCESS

- ○ Calcium imaging
- ○ Photo-activated localization microscopy (PALM)
- ○ Direct Stochastic Optical Reconstruction Microscopy (dSTORM)
- ○ Fluorescence recovery after photobleaching (FRAP)
- ○ Frequency domain based fluorescence lifetime imaging microscopy of Förster resonance energy transfer (FLIM-FRET)
- ○ Single particle tracking (SPT)
- ● QUANTIFICATION AND STATISTICAL ANALYSIS

SUPPLEMENTAL INFORMATION

Supplemental information can be found online at https://doi.org/10.1016/j.neuron.2024.06.028.

AUTHOR CONTRIBUTIONS

F.V., A.F., J.J., S.Z., L.B., and J.P.D. performed and analyzed SPT experiments. F.V., A.F., J.J., N.B., and J.P.D. performed and analyzed FLIM-FRET experiments. A.F. performed and analyzed calcium imaging and spine counting experiments. F.U. performed and analyzed PALM experiments. F.V. performed and analyzed FRAP experiments. A.F. and S.Z. performed and analyzed STORM experiments. A.F. and F.V. performed and analyzed immunocytochemistry experiments. F.V., H.G., and O.N. performed surgeries and behavioral experiments and analysis. D.B. and L.V. generated molecular biology constructs. V.R. and J.H. performed clinical assessments, purified immunoglobulins, and provided patient samples. J.P.D. and L.G. acquired the funding, conceived and supervised the project, designed the experiments, and wrote the manuscript with input from co-authors.

DECLARATION OF INTERESTS

The authors declare that they have no competing interests.

REFERENCES

1. Paoletti, P., Bellone, C., and Zhou, Q. (2013). NMDA receptor subunit diversity: impact on receptor properties, synaptic plasticity and disease. Nat. Rev. Neurosci. *14*, 383–400. https://doi.org/10.1038/nrn3504.

2. Hansen, K.B., Wollmuth, L.P., Bowie, D., Furukawa, H., Menniti, F.S., Sobolevsky, A.I., Swanson, G.T., Swanger, S.A., Greger, I.H., Nakagawa, T., et al. (2021). Structure, Function, and Pharmacology of Glutamate Receptor Ion Channels. Pharmacol. Rev. *73*, 298–487. https://doi.org/10.1124/pharmrev.120.000131.

3. Park, D.K., Stein, I.S., and Zito, K. (2022). Ion flux-independent NMDA receptor signaling. Neuropharmacology *210*, 109019. https://doi.org/10.1016/j.neuropharm.2022.109019.

4. Dore, K., Stein, I.S., Brock, J.A., Castillo, P.E., Zito, K., and Sjöström, P.J. (2017). Unconventional NMDA Receptor Signaling. J. Neurosci. *37*, 10800–10807. https://doi.org/10.1523/JNEUROSCI.1825-17.2017.

5. Stein, I.S., Gray, J.A., and Zito, K. (2015). Non-Ionotropic NMDA Receptor Signaling Drives Activity-Induced Dendritic Spine Shrinkage. J. Neurosci. *35*, 12303–12308. https://doi.org/10.1523/JNEUROSCI.4289-14.2015.

6. Stein, I.S., Park, D.K., Claiborne, N., and Zito, K. (2021). Non-ionotropic NMDA receptor signaling gates bidirectional structural plasticity of dendritic spines. Cell Rep. *34*, 108664. https://doi.org/10.1016/j.celrep.2020.108664.

7. Dupuis, J.P., Ladépêche, L., Seth, H., Bard, L., Varela, J., Mikasova, L., Bouchet, D., Rogemond, V., Honnorat, J., Hanse, E., et al. (2014). Surface dynamics of GluN2B-NMDA receptors controls plasticity of maturing glutamate synapses. EMBO J. *33*, 842–861. https://doi.org/10.1002/embj.201386356.

8. Kellermayer, B., Ferreira, J.S., Dupuis, J., Levet, F., Grillo-Bosch, D., Bard, L., Linarès-Loyez, J., Bouchet, D., Choquet, D., Rusakov, D.A., et al. (2018). Differential Nanoscale Topography and Functional Role of GluN2-NMDA Receptor Subtypes at Glutamatergic Synapses. Neuron *100*, 106–119.e7. https://doi.org/10.1016/j.neuron.2018.09.012.

9. Li, L., and Hanahan, D. (2013). Hijacking the neuronal NMDAR signaling circuit to promote tumor growth and invasion. Cell *153*, 86–100. https://doi.org/10.1016/j.cell.2013.02.051.

10. Zeng, Q., Michael, I.P., Zhang, P., Saghafinia, S., Knott, G., Jiao, W., McCabe, B.D., Galván, J.A., Robinson, H.P.C., Zlobec, I., et al. (2019). Synaptic proximity enables NMDAR signalling to promote brain metastasis. Nature *573*, 526–531. https://doi.org/10.1038/s41586-019-1576-6.

11. Marquard, J., Otter, S., Welters, A., Stirban, A., Fischer, A., Eglinger, J., Herebian, D., Kletke, O., Klemen, M.S., Stožer, A., et al. (2015). Characterization of pancreatic NMDA receptors as possible drug targets for diabetes treatment. Nat. Med. *21*, 363–372. https://doi.org/10.1038/nm.3822.

12. Dalmau, J., and Graus, F. (2018). Antibody-Mediated Encephalitis. N. Engl. J. Med. *378*, 840–851. https://doi.org/10.1056/NEJMra1708712.

13. Hughes, E.G., Peng, X., Gleichman, A.J., Lai, M., Zhou, L., Tsou, R., Parsons, T.D., Lynch, D.R., Dalmau, J., and Balice-Gordon, R.J. (2010). Cellular and synaptic mechanisms of anti-NMDA receptor encephalitis. J. Neurosci. *30*, 5866–5875. https://doi.org/10.1523/JNEUROSCI.0167-10.2010.

14. Dalmau, J., Armangué, T., Planagumà, J., Radosevic, M., Mannara, F., Leypoldt, F., Geis, C., Lancaster, E., Titulaer, M.J., Rosenfeld, M.R., et al. (2019). An update on anti-NMDA receptor encephalitis for neurologists and psychiatrists: mechanisms and models. Lancet Neurol. *18*, 1045–1057. https://doi.org/10.1016/S1474-4422(19)30244-3.

15. Gleichman, A.J., Spruce, L.A., Dalmau, J., Seeholzer, S.H., and Lynch, D.R. (2012). Anti-NMDA receptor encephalitis antibody binding is dependent on amino acid identity of a small region within the GluN1 amino terminal domain. J. Neurosci. *32*, 11082–11094. https://doi.org/10.1523/JNEUROSCI.0064-12.2012.

16. Ladépêche, L., Planagumà, J., Thakur, S., Suárez, I., Hara, M., Borbely, J.S., Sandoval, A., Laparra-Cuervo, L., Dalmau, J., and Lakadamyali, M. (2018). NMDA Receptor Autoantibodies in Autoimmune Encephalitis Cause a Subunit-Specific Nanoscale Redistribution of NMDA Receptors. Cell Rep. 23, 3759–3768. https://doi.org/10.1016/j.celrep.2018.05.096.

17. Mikasova, L., De Rossi, P., Bouchet, D., Georges, F., Rogemond, V., Didelot, A., Meissirel, C., Honnorat, J., and Groc, L. (2012). Disrupted surface cross-talk between NMDA and Ephrin-B2 receptors in anti-NMDA encephalitis. Brain 135, 1606–1621. https://doi.org/10.1093/brain/aws092.

18. Dean, C.A., Metzbower, S.R., Dessain, S.K., Blanpied, T.A., and Benavides, D.R. (2022). Regulation of NMDA Receptor Signaling at Single Synapses by Human Anti-NMDA Receptor Antibodies. Front. Mol. Neurosci. 15, 940005. https://doi.org/10.3389/fnmol.2022.940005.

19. Jézéquel, J., Johansson, E.M., Dupuis, J.P., Rogemond, V., Gréa, H., Kellermayer, B., Hamdani, N., Le Guen, E., Rabu, C., Lepleux, M., et al. (2017). Dynamic disorganization of synaptic NMDA receptors triggered by autoantibodies from psychotic patients. Nat. Commun. 8, 1791. https://doi.org/10.1038/s41467-017-01700-3.

20. Ceanga, M., Rahmati, V., Haselmann, H., Schmidl, L., Hunter, D., Brauer, A.K., Liebscher, S., Kreye, J., Prüss, H., Groc, L., et al. (2023). Human NMDAR autoantibodies disrupt excitatory-inhibitory balance, leading to hippocampal network hypersynchrony. Cell Rep. 42, 113166. https://doi.org/10.1016/j.celrep.2023.113166.

21. Hunter, D., Petit-Pedrol, M., Fernandes, D., Bénac, N., Rodrigues, C., Kreye, J., Ceanga, M., Prüss, H., Geis, C., and Groc, L. (2024). Converging synaptic and network dysfunctions in distinct autoimmune encephalitis. EMBO Rep. 25, 1623–1649. https://doi.org/10.1038/s44319-024-00056-2.

22. Lipton, S.A. (2006). Paradigm shift in neuroprotection by NMDA receptor blockade: memantine and beyond. Nat. Rev. Drug Discov. 5, 160–170. https://doi.org/10.1038/nrd1958.

23. Murrough, J.W., Abdallah, C.G., and Mathew, S.J. (2017). Targeting glutamate signalling in depression: progress and prospects. Nat. Rev. Drug Discov. 16, 472–486. https://doi.org/10.1038/nrd.2017.16.

24. Millan, M.J., Andrieux, A., Bartzokis, G., Cadenhead, K., Dazzan, P., Fusar-Poli, P., Gallinat, J., Giedd, J., Grayson, D.R., Heinrichs, M., et al. (2016). Altering the course of schizophrenia: progress and perspectives. Nat. Rev. Drug Discov. 15, 485–515. https://doi.org/10.1038/nrd.2016.28.

25. Zhang, W., Ross, P.J., Ellis, J., and Salter, M.W. (2022). Targeting NMDA receptors in neuropsychiatric disorders by drug screening on human neurons derived from pluripotent stem cells. Transl. Psychiatry 12, 243. https://doi.org/10.1038/s41398-022-02010-z.

26. Cadinu, D., Grayson, B., Podda, G., Harte, M.K., Doostdar, N., and Neill, J.C. (2018). NMDA receptor antagonist rodent models for cognition in schizophrenia and identification of novel drug treatments, an update. Neuropharmacology 142, 41–62. https://doi.org/10.1016/j.neuropharm.2017.11.045.

27. Krystal, J.H., Abdallah, C.G., Sanacora, G., Charney, D.S., and Duman, R.S. (2019). Ketamine: A Paradigm Shift for Depression Research and Treatment. Neuron 101, 774–778. https://doi.org/10.1016/j.neuron.2019.02.005.

28. Potier, M., Georges, F., Brayda-Bruno, L., Ladépêche, L., Lamothe, V., Abed, S.A., Groc, L., and Marighetto, A. (2016). Temporal memory and its enhancement by estradiol requires surface dynamics of hippocampal CA1 NMDA receptors. Biol. Psychiatry 79, 735–745. https://doi.org/10.1016/j.biopsych.2015.07.017.

29. Dupuis, J.P., Nicole, O., and Groc, L. (2023). NMDA receptor functions in health and disease: Old actor, new dimensions. Neuron 111, 2312–2328. https://doi.org/10.1016/j.neuron.2023.05.002.

30. Dore, K., Aow, J., and Malinow, R. (2015). Agonist binding to the NMDA receptor drives movement of its cytoplasmic domain without ion flow. Proc. Natl. Acad. Sci. USA 112, 14705–14710. https://doi.org/10.1073/pnas.1520023112.

31. Ferreira, J.S., Papouin, T., Ladépêche, L., Yao, A., Langlais, V.C., Bouchet, D., Dulong, J., Mothet, J.-P., Sacchi, S., Pollegioni, L., et al. (2017). Co-agonists differentially tune GluN2B-NMDA receptor trafficking at hippocampal synapses. eLife 6, e25492. https://doi.org/10.7554/eLife.25492.

32. Doré, K., Labrecque, S., Tardif, C., and De Koninck, P. (2014). FRET-FLIM investigation of PSD95-NMDA receptor interaction in dendritic spines; control by calpain, CaMKII and Src family kinase. PLoS One 9, e112170. https://doi.org/10.1371/journal.pone.0112170.

33. Zhang, Y., Ye, F., Zhang, T., Lv, S., Zhou, L., Du, D., Lin, H., Guo, F., Luo, C., and Zhu, S. (2021). Structural basis of ketamine action on human NMDA receptors. Nature 596, 301–305. https://doi.org/10.1038/s41586-021-03769-9.

34. Elias, G.M., and Nicoll, R.A. (2007). Synaptic trafficking of glutamate receptors by MAGUK scaffolding proteins. Trends Cell Biol. 17, 343–352.

35. Bard, L., Sainlos, M., Bouchet, D., Cousins, S., Mikasova, L., Breillat, C., Stephenson, F.A., Imperiali, B., Choquet, D., and Groc, L. (2010). Dynamic and specific interaction between synaptic NR2-NMDA receptor and PDZ proteins. Proc. Natl. Acad. Sci. USA 107, 19561–19566. https://doi.org/10.1073/pnas.1002690107.

36. Dalmau, J., Geis, C., and Graus, F. (2017). Autoantibodies to Synaptic Receptors and Neuronal Cell Surface Proteins in Autoimmune Diseases of the Central Nervous System. Physiol. Rev. 97, 839–887. https://doi.org/10.1152/physrev.00010.2016.

37. Wollmuth, L.P., Chan, K., and Groc, L. (2021). The diverse and complex modes of action of anti-NMDA receptor autoantibodies. Neuropharmacology 194, 108624. https://doi.org/10.1016/j.neuropharm.2021.108624.

38. Lee, S.J.R., Escobedo-Lozoya, Y., Szatmari, E.M., and Yasuda, R. (2009). Activation of CaMKII in single dendritic spines during long-term potentiation. Nature 458, 299–304. https://doi.org/10.1038/nature07842.

39. Planagumà, J., Leypoldt, F., Mannara, F., Gutiérrez-Cuesta, J., Martín-García, E., Aguilar, E., Titulaer, M.J., Petit-Pedrol, M., Jain, A., Balice-Gordon, R., et al. (2015). Human N-methyl D-aspartate receptor antibodies alter memory and behaviour in mice. Brain 138, 94–109. https://doi.org/10.1093/brain/awu310.

40. Song, X., Jensen, M.Ø., Jogini, V., Stein, R.A., Lee, C.H., McHaourab, H.S., Shaw, D.E., and Gouaux, E. (2018). Mechanism of NMDA receptor channel block by MK-801 and memantine. Nature 556, 515–519. https://doi.org/10.1038/s41586-018-0039-9.

41. Yasuda, R., Hayashi, Y., and Hell, J.W. (2022). CaMKII: a central molecular organizer of synaptic plasticity, learning and memory. Nat. Rev. Neurosci. 23, 666–682. https://doi.org/10.1038/s41583-022-00624-2.

42. Ferreira, J.S., Dupuis, J.P., Kellermayer, B., Bénac, N., Manso, C., Bouchet, D., Levet, F., Butler, C., Sibarita, J.B., and Groc, L. (2020). Distance-dependent regulation of NMDAR nanoscale organization along hippocampal neuron dendrites. Proc. Natl. Acad. Sci. USA 117, 24526–24533. https://doi.org/10.1073/pnas.1922477117.

43. Hosokawa, T., Liu, P.W., Cai, Q., Ferreira, J.S., Levet, F., Butler, C., Sibarita, J.B., Choquet, D., Groc, L., Hosy, E., et al. (2021). CaMKII activation persistently segregates postsynaptic proteins via liquid phase separation. Nat. Neurosci. 24, 777–785. https://doi.org/10.1038/s41593-021-00843-3.

44. Casarotto, P.C., Girych, M., Fred, S.M., Kovaleva, V., Moliner, R., Enkavi, G., Biojone, C., Cannarozzo, C., Sahu, M.P., Kaurinkoski, K., et al. (2021). Antidepressant drugs act by directly binding to TRKB neurotrophin receptors. Cell 184, 1299–1313.e19. https://doi.org/10.1016/j.cell.2021.01.034.

45. Lasič, E., Lisjak, M., Horvat, A., Božić, M., Šakanović, A., Anderluh, G., Verkhratsky, A., Vardjan, N., Jorgačevski, J., Stenovec, M., et al. (2019). Astrocyte Specific Remodeling of Plasmalemmal Cholesterol Composition by Ketamine Indicates a New Mechanism of Antidepressant Action. Sci. Rep. 9, 10957. https://doi.org/10.1038/s41598-019-47459-z.

Neuron
Article

CellPress
OPEN ACCESS

46. Wilcox, M.R., Nigam, A., Glasgow, N.G., Narangoda, C., Phillips, M.B., Patel, D.S., Mesbahi-Vasey, S., Turcu, A.L., Vázquez, S., Kurnikova, M.G., et al. (2022). Inhibition of NMDA receptors through a membrane-to-channel path. Nat. Commun. *13*, 4114. https://doi.org/10.1038/s41467-022-31817-z.

47. Thompson, R.J., Jackson, M.F., Olah, M.E., Rungta, R.L., Hines, D.J., Beazely, M.A., MacDonald, J.F., and MacVicar, B.A. (2008). Activation of pannexin-1 hemichannels augments aberrant bursting in the hippocampus. Science *322*, 1555–1559. https://doi.org/10.1126/science.1165209.

48. Weilinger, N.L., Lohman, A.W., Rakai, B.D., Ma, E.M.M., Bialecki, J., Maslieieva, V., Rilea, T., Bandet, M.V., Ikuta, N.T., Scott, L., et al. (2016). Metabotropic NMDA receptor signaling couples Src family kinases to pannexin-1 during excitotoxicity. Nat. Neurosci. *19*, 432–442. https://doi.org/10.1038/nn.4236.

49. Yan, J., Bengtson, C.P., Buchthal, B., Hagenston, A.M., and Bading, H. (2020). Coupling of NMDA receptors and TRPM4 guides discovery of unconventional neuroprotectants. Science *370*, eaay3302. https://doi.org/10.1126/science.aay3302.

50. Zong, P., Feng, J., Yue, Z., Li, Y., Wu, G., Sun, B., He, Y., Miller, B., Yu, A.S., Su, Z., et al. (2022). Functional coupling of TRPM2 and extrasynaptic NMDARs exacerbates excitotoxicity in ischemic brain injury. Neuron *110*, 1944–1958.e8. https://doi.org/10.1016/j.neuron.2022.03.021.

51. Gardoni, F., Picconi, B., Ghiglieri, V., Polli, F., Bagetta, V., Bernardi, G., Cattabeni, F., Di Luca, M., and Calabresi, P. (2006). A critical interaction between NR2B and MAGUK in L-DOPA induced dyskinesia. J. Neurosci. *26*, 2914–2922.

52. Milnerwood, A.J., Gladding, C.M., Pouladi, M.A., Kaufman, A.M., Hines, R.M., Boyd, J.D., Ko, R.W.Y., Vasuta, O.C., Graham, R.K., Hayden, M.R., et al. (2010). Early increase in extrasynaptic NMDA receptor signaling and expression contributes to phenotype onset in Huntington's disease mice. Neuron *65*, 178–190. https://doi.org/10.1016/j.neuron.2010.01.008.

53. Cissé, M., Halabisky, B., Harris, J., Devidze, N., Dubal, D.B., Sun, B., Orr, A., Lotz, G., Kim, D.H., Hamto, P., et al. (2011). Reversing EphB2 depletion rescues cognitive functions in Alzheimer model. Nature *469*, 47–52. https://doi.org/10.1038/nature09635.

54. Lacor, P.N., Buniel, M.C., Furlow, P.W., Clemente, A.S., Velasco, P.T., Wood, M., Viola, K.L., and Klein, W.L. (2007). Abeta oligomer-induced aberrations in synapse composition, shape, and density provide a molecular basis for loss of connectivity in Alzheimer's disease. J. Neurosci. *27*, 796–807. https://doi.org/10.1523/JNEUROSCI.3501-06.2007.

55. Birnbaum, J.H., Bali, J., Rajendran, L., Nitsch, R.M., and Tackenberg, C. (2015). Calcium flux-independent NMDA receptor activity is required for Abeta oligomer-induced synaptic loss. Cell Death Dis. *6*, e1791. https://doi.org/10.1038/cddis.2015.160.

56. Dore, K., Carrico, Z., Alfonso, S., Marino, M., Koymans, K., Kessels, H.W., and Malinow, R. (2021). PSD-95 protects synapses from beta-amyloid. Cell Rep. *35*, 109194. https://doi.org/10.1016/j.celrep.2021.109194.

57. Kessels, H.W., Nabavi, S., and Malinow, R. (2013). Metabotropic NMDA receptor function is required for beta-amyloid-induced synaptic depression. Proc. Natl. Acad. Sci. USA *110*, 4033–4038. https://doi.org/10.1073/pnas.1219605110.

58. Tamburri, A., Dudilot, A., Licea, S., Bourgeois, C., and Boehm, J. (2013). NMDA-receptor activation but not ion flux is required for amyloid-beta induced synaptic depression. PLoS One *8*, e65350. https://doi.org/10.1371/journal.pone.0065350.

59. Jézéquel, J., Lepleux, M., Kahn, R.S., Honnorat, J., Leboyer, M., and Groc, L. (2018). Molecular Pathogenicity of Anti-NMDA Receptor Autoantibody From Patients With First-Episode Psychosis. Am. J. Psychiatry *175*, 382–383.

60. Planagumà, J., Haselmann, H., Mannara, F., Petit-Pedrol, M., Grünewald, B., Aguilar, E., Röpke, L., Martín-García, E., Titulaer, M.J., Jercog, P., et al. (2016). Ephrin-B2 prevents N-methyl-D-aspartate receptor antibody ef-

fects on memory and neuroplasticity. Ann. Neurol. *80*, 388–400. https://doi.org/10.1002/ana.24721.

61. Espana, A., Seth, H., Jézéquel, J., Huang, T., Bouchet, D., Lepleux, M., Gréa, H., Bechter, K., Schneider, M., Hanse, E., et al. (2021). Alteration of NMDA receptor trafficking as a cellular hallmark of psychosis. Transl. Psychiatry *11*, 444. https://doi.org/10.1038/s41398-021-01549-7.

62. Johansson, E.M., Bouchet, D., Tamouza, R., Ellul, P., Morr, A.S., Avignone, E., Germi, R., Leboyer, M., Perron, H., and Groc, L. (2020). Human endogenous retroviral protein triggers deficit in glutamate synapse maturation and behaviors associated with psychosis. Sci. Adv. *6*, eabc0708. https://doi.org/10.1126/sciadv.abc0708.

63. Duman, R.S., Aghajanian, G.K., Sanacora, G., and Krystal, J.H. (2016). Synaptic plasticity and depression: new insights from stress and rapid-acting antidepressants. Nat. Med. *22*, 238–249. https://doi.org/10.1038/nm.4050.

64. Gould, T.D., Zarate, C.A., Jr., and Thompson, S.M. (2019). Molecular Pharmacology and Neurobiology of Rapid-Acting Antidepressants. Annu. Rev. Pharmacol. Toxicol. *59*, 213–236. https://doi.org/10.1146/annurev-pharmtox-010617-052811.

65. Castrén, E., and Monteggia, L.M. (2021). Brain-Derived Neurotrophic Factor Signaling in Depression and Antidepressant Action. Biol. Psychiatry *90*, 128–136. https://doi.org/10.1016/j.biopsych.2021.05.008.

66. Moliner, R., Girych, M., Brunello, C.A., Kovaleva, V., Biojone, C., Enkavi, G., Antenucci, L., Kot, E.F., Goncharuk, S.A., Kaurinkoski, K., et al. (2023). Psychedelics promote plasticity by directly binding to BDNF receptor TrkB. Nat. Neurosci. *26*, 1032–1041. https://doi.org/10.1038/s41593-023-01316-5.

67. Zhang, H., Etherington, L.A., Hafner, A.S., Belelli, D., Coussen, F., Delagrange, P., Chaouloff, F., Spedding, M., Lambert, J.J., Choquet, D., et al. (2013). Regulation of AMPA receptor surface trafficking and synaptic plasticity by a cognitive enhancer and antidepressant molecule. Mol. Psychiatry *18*, 471–484. https://doi.org/10.1038/mp.2012.80.

68. Fred, S.M., Moliner, R., Antila, H., Engelhardt, K.A., Schlüter, O.M., Casarotto, P.C., and Castrén, E. (2023). TRKB interaction with PSD95 is associated with latency of fluoxetine and 2R,6R-hydroxynorketamine. Eur. J. Neurosci. *57*, 1215–1224. https://doi.org/10.1111/ejn.15952.

69. Xue, S.G., He, J.G., Lu, L.L., Song, S.J., Chen, M.M., Wang, F., and Chen, J.G. (2023). Enhanced TARP-γ8-PSD-95 coupling in excitatory neurons contributes to the rapid antidepressant-like action of ketamine in male mice. Nat. Commun. *14*, 7971. https://doi.org/10.1038/s41467-023-42780-8.

70. Su, T., Lu, Y., Fu, C., Geng, Y., and Chen, Y. (2023). GluN2A mediates ketamine-induced rapid antidepressant-like responses. Nat. Neurosci. *26*, 1751–1761. https://doi.org/10.1038/s41593-023-01436-y.

71. Ma, S., Chen, M., Jiang, Y., Xiang, X., Wang, S., Wu, Z., Li, S., Cui, Y., Wang, J., Zhu, Y., et al. (2023). Sustained antidepressant effect of ketamine through NMDAR trapping in the LHb. Nature *622*, 802–809. https://doi.org/10.1038/s41586-023-06624-1.

72. Yang, Y., Cui, Y., Sang, K., Dong, Y., Ni, Z., Ma, S., and Hu, H. (2018). Ketamine blocks bursting in the lateral habenula to rapidly relieve depression. Nature *554*, 317–322. https://doi.org/10.1038/nature25509.

73. Prybylowski, K., Chang, K., Sans, N., Kan, L., Vicini, S., and Wenthold, R.J. (2005). The synaptic localization of NR2B-containing NMDA receptors is controlled by interactions with PDZ proteins and AP-2. Neuron *47*, 845–857.

74. Jacob, T.C., Bogdanov, Y.D., Magnus, C., Saliba, R.S., Kittler, J.T., Haydon, P.G., and Moss, S.J. (2005). Gephyrin regulates the cell surface dynamics of synaptic GABAA receptors. J. Neurosci. *25*, 10469–10478. https://doi.org/10.1523/JNEUROSCI.2267-05.2005.

75. Chen, T.W., Wardill, T.J., Sun, Y., Pulver, S.R., Renninger, S.L., Baohan, A., Schreiter, E.R., Kerr, R.A., Orger, M.B., Jayaraman, V., et al. (2013). Ultrasensitive fluorescent proteins for imaging neuronal activity. Nature *499*, 295–300. https://doi.org/10.1038/nature12354.

76. Hanus, C., Ehrensperger, M.V., and Triller, A. (2006). Activity-dependent movements of postsynaptic scaffolds at inhibitory synapses. J. Neurosci. *26*, 4586–4595. https://doi.org/10.1523/JNEUROSCI.5123-05.2006.

77. Butler, C., Saraceno, G.E., Kechkar, A., Bénac, N., Studer, V., Dupuis, J.P., Groc, L., Galland, R., and Sibarita, J.B. (2022). Multi-Dimensional Spectral Single Molecule Localization Microscopy. Front. Bioinform. *2*, 813494. https://doi.org/10.3389/fbinf.2022.813494.

78. Kechkar, A., Nair, D., Heilemann, M., Choquet, D., and Sibarita, J.B. (2013). Real-time analysis and visualization for single-molecule based super-resolution microscopy. PLoS One *8*, e62918. https://doi.org/10.1371/journal.pone.0062918.

79. Levet, F., Hosy, E., Kechkar, A., Butler, C., Beghin, A., Choquet, D., and Sibarita, J.B. (2015). SR-Tesseler: a method to segment and quantify localization-based super-resolution microscopy data. Nat. Methods *12*, 1065–1071. https://doi.org/10.1038/nmeth.3579.

80. Johansson, E.M., Bouchet, D., Tamouza, R., Ellul, P., Morr, A.S., A., E., Germi, R., Leboyer, M., Perron, H., et al. (2020). Human endogenous retroviral protein triggers deficit in glutamate synapse maturation and behaviors associated to psychosis. Sci. Adv. *6*, eabc0708.

81. Viaccoz, A., Desestret, V., Ducray, F., Picard, G., Cavillon, G., Rogemond, V., Antoine, J.C., Delattre, J.Y., and Honnorat, J. (2014). Clinical specific-ities of adult male patients with NMDA receptor antibodies encephalitis. Neurology *82*, 556–563. https://doi.org/10.1212/WNL.0000000000000126.

82. Kaech, S., and Banker, G. (2006). Culturing hippocampal neurons. Nat. Protoc. *1*, 2406–2415. https://doi.org/10.1038/nprot.2006.356.

83. Guilloux, J.P., Seney, M., Edgar, N., and Sibille, E. (2011). Integrated behavioral z-scoring increases the sensitivity and reliability of behavioral phenotyping in mice: relevance to emotionality and sex. J. Neurosci. Methods *197*, 21–31. https://doi.org/10.1016/j.jneumeth.2011.01.019.

84. Heilemann, M., van de Linde, S., Schüttpelz, M., Kasper, R., Seefeldt, B., Mukherjee, A., Tinnefeld, P., and Sauer, M. (2008). Subdiffraction-reso-lution fluorescence imaging with conventional fluorescent probes. Angew. Chem. Int. Ed. Engl. *47*, 6172–6176. https://doi.org/10.1002/anie.200802376.

85. Aow, J., Dore, K., and Malinow, R. (2015). Conformational signaling required for synaptic plasticity by the NMDA receptor complex. Proc. Natl. Acad. Sci. USA *112*, 14711–14716. https://doi.org/10.1073/pnas.1520029112.

86. Mannara, F., Radosevic, M., Planagumà, J., Soto, D., Aguilar, E., García-Serra, A., Maudes, E., Pedreño, M., Paul, S., Doherty, J., et al. (2020). Allosteric modulation of NMDA receptors prevents the antibody effects of patients with anti-NMDAR encephalitis. Brain *143*, 2709–2720. https://doi.org/10.1093/brain/awaa195.

CellPress
OPEN ACCESS

STAR★METHODS

KEY RESOURCES TABLE

REAGENT or RESOURCE	SOURCE	IDENTIFIER
Antibodies		
Anti-GFP polyclonal antibody (rabbit)	ThermoFisher Scientific	Cat# A-6455
Anti-GluN1 polyclonal antibody (rabbit)	Alomone Labs	Cat# AGC-001
Anti-K$_V$1.3 polyclonal antibody (rabbit)	Alomone Labs	Cat# APC-101
Anti-EphB2R polyclonal antibody (goat)	R&D systems	Cat# AF467
Anti-Flag polyclonal antibody (rabbit)	Sigma-Aldrich	Cat# F2555
Anti-Flag M2 monoclonal antibody (mouse)	Sigma-Aldrich	Cat# F1804
Anti-GluN2B polyclonal antibody (rabbit)	Alomone Labs	Cat# AGC-003
Anti-GluN2B polyclonal antibody (rabbit)	Homemade[8]	N/A
Anti-Homer1 polyclonal antibody (guinea pig)	Synaptic Systems	#AB 10549720
Anti-GFP polyclonal antibody (mouse)	Roche	Cat# 11814460001
Alexa 594-conjugated anti-guinea pig (goat)	Jackson ImmunoResearch	#AB_2337442
Alexa 488-conjugated anti-mouse secondary antibody (goat)	ThermoFisher Scientific	CAT#A28175
Alexa Fluor 647-conjugated anti-mouse IgG (donkey)	ThermoFisher Scientific	Cat# A31571
Qdot 655-conjugated anti-rabbit IgG (goat)	ThermoFisher Scientific	Cat# Q11422MP
Qdot 655-conjugated anti-goat IgG (rabbit)	ThermoFisher Scientific	Cat# Q11821MP
Chemicals, peptides, and recombinant proteins		
Buprenorphine	Axience	Buprecare (0.3 mg/ml)
Meloxicam	Boehringer Ingelheim Animal Health France	Metacam (0.5 mg/m)
Ketamine hydrochloride	Virbac	Ketamine 1000 (100 mg/ml)
D-AP5	Tocris Bioscience	Cat# 0106
(+)-MK-801 maleate	Tocris Bioscience	Cat# 0924
Memantine hydrochloride	Tocris Bioscience	Cat# 0773
(RS)-CPP	Tocris Bioscience	Cat# 0173
Kynurenic acid	Sigma-Aldrich	Cat# K3375
NMDA	Sigma-Aldrich	Cat# M3262
Poly-L-lysine	Sigma-Aldrich	Cat# P4707
Horse serum	ThermoFisher Scientific	Waltham, MA, USA, ref. N° 26050-88
Bovine serum albumin (BSA)	Sigma-Aldrich	Cat #A3059
Fluoromount-G mounting medium containing DAPI	ThermoFisher Scientific	Cat #00-4959-52
Mowiol mounting medium	Sigma-Aldrich	Ref. #475904
Poly-L-lysine	Sigma-Aldrich	Ref. #P26361G
Neurobasal medium/B27	ThermoFisher Scientific	Ref. #12348-017/A3582901
NeuroCult SM1	Stemcell technologies	CAT#05711
BrainPhys medium	Stemcell technologies	CAT#05790
Leibovitz's L-15 medium	ThermoFisher Scientific	CAT#11415064
Hank's Balanced Salt Solution	ThermoFisher Scientific	Ref. #25300-054
Glycerol 24%	Sigma-Aldrich	Ref. #G5516
Tris-Cl	Sigma-Aldrich	CAT#15,456-3
TetraSpeck microspheres	ThermoFisher Scientific	Cat# T7279
Biomimetic TAT-2B peptide (YGRKKRRQRRRNGHVYEKLSSIESDV)	CASLO ApS	N/A
Non-sense TAT-NS peptide (YGRKKRRQRRRGSEVILDQPVIAKPLIPALSVALSVKEEA)	CASLO ApS	N/A

(Continued on next page)

Continued

REAGENT or RESOURCE	SOURCE	IDENTIFIER
Recombinant DNA		
Plasmid to express mEos3.2-GluN1 (pRcCMV-mEos3.2-GluN1)	Homemade (this paper)	N/A
Plasmid to express GFP-Homer1c (pcDNA3.1-EGFP-Homer1c)	Homemade[35]	N/A
Plasmid to express dimeric DsRed-Homer1c (pcDNA3.1-dimeric_DsRed-Homer1c)	Homemade[35]	N/A
Plasmid to express GluN1-mCherry (pCMV-GluN1-mCherry)	Gift from P. de Koninck[30]	N/A
Plasmid to express GluN1-mGFP (pCMV-GluN1-mGFP)	Gift from P. de Koninck[32]	N/A
Plasmid to express GluN1-N616A-mGFP (pCMV-GluN1-N616A-mGFP)	Homemade (this paper)	N/A
Plasmid to express GluN1-N616A-mCherry (pCMV-GluN1-N616A-mCherry)	Homemade (this paper)	N/A
Plasmid to express Flag-GluN1 (pCMV-Flag-GluN1)	Homemade[35]	N/A
Plasmid to express Flag-GluN2B (pCMV-Flag-GluN2B)	Gift from R. Wenthold[73]	N/A
Plasmid to express PSD-95-mCherry (pCMV-PSD-95-mCherry)	Gift from P. de Koninck[32]	N/A
Plasmid to express Green-Camuiα	Addgene[38]	pCMV-REACh-CaMKIIa-mEGFP #26933
Plasmid to express SEP-γ2 (pCMV-SEP-γ2-GABA$_A$R)	Gift from S. Moss[74]	N/A
Plasmid to express Flag-GluN2A-S1462A (pCMV-Flag-GluN2A-S1462A)	Gift from R. Wenthold[73]	N/A
Plasmid to express Flag-GluN2B-S1480A (pCMV-Flag-GluN2B-S1480A)	Gift from R. Wenthold[73]	N/A
Plasmid to express SEP-GluN2A (pCMV-SEP-GluN2A)	Homemade[35]	N/A
Plasmid to express GCaMP6f (pZac2.1-GCaMP6f)	Gift from B. Khakh[75]	N/A
Plasmid to express mVenus-Gephyrin (pCMV-mVenus-Gephyrin)	Gift from A. Triller[76]	N/A
Experimental models: Organisms/strains		
Sprague-Dawley rats (RjHan:SD)	Janvier Labs	N/A
Software and algorithms		
GraphPad Prism v8.0	GraphPad	https://www.graphpad.com/
MetaMorph v7.8	Molecular Devices	https://www.moleculardevices.com/products/cellular-imaging-systems/acquisition-and-analysis-software/metamorph-microscopy
PALMTracer	Sibarita's Lab[77]	https://www.iins.u-bordeaux.fr/projectSIBARITA70
WaveTracer	Sibarita's lab[78]	https://www.iins.u-bordeaux.fr/projectSIBARITA37
SR Tesseler	Sibarita's lab[79]	https://github.com/flevet/SR-Tesseler
MatLab	MathWorks	https://fr.mathworks.com/products/matlab.html
ImageJ	National Institutes of Health	https://imagej.nih.gov/ij/download.html
LI-FLIM	Lambert Instruments	https://www.lambertinstruments.com/liflim
EthoVision XT	Noldus	https://www.noldus.com/ethovision-xt
Other		
Osmotic pumps	Alzet	Model 2002
Forced Swim test	Noldus	N/A
Elevated plus maze	Noldus	N/A
Open-field arena	Homemade[80]	N/A
Panlab startle chamber	Harvard Apparatus	76-0280

Neuron
Article

CellPress
OPEN ACCESS

RESOURCE AVAILABILITY

Lead contact
Further information and requests for resources and reagents should be directed to Laurent Groc (laurent.groc@u-bordeaux.fr).

Materials availability
All unique/stable reagents generated in this study are available from the lead contact without restriction.

Data and code availability
- All data reported in this paper will be shared by the lead contact upon request.
- Code: This paper does not report original code.
- Any additional information required to reanalyze the data reported in this paper is available from the lead contact upon request.

EXPERIMENTAL MODEL AND SUBJECT DETAILS

Human samples
Purified immunoglobulins (IgG) and cerebrospinal fluid (CSF) samples were collected from patients with anti-NMDAR encephalitis (no demographic information available) at the national reference center for auto-immune neurological diseases (Pr J. Honnorat, Lyon; governmental authorization for biological material collection n° AC-20152576) upon early symptom presentation before any treatment was administrated. They were stored at -80°C (biological material storage declaration n° DC-2008-72; CNIL number of the tumorotek database for anonymized biological material handling n°1128997) at the NeuroBioTec center for biological ressources of the Hospices Civils de Lyon (CRB-HCL, NF 96-900 certified, accreditation number BB-0033-00046; Lyon, France). Analysis on patient CSF included detection of NMDAR-IgG and titration of cell counts, proteins, glucose, as well as CSF/serum albumin ratio which is an indicator of blood-brain barrier impairment. Patients also underwent a tumor screening. Serum samples were tested for the presence of NMDAR-IgG using a cell-based assay on human embryonic kidney cells (HEK293) expressing both GluN1- and GluN2B-NMDAR subunits, as previously described.[17,81] To detect NMDAR-IgG in CSF samples, cells were fixed (4% PFA, 10 min) and incubated with patient CSF (1:50 dilution in saturation buffer, 90 min). Samples were considered as positive when a clear staining was confirmed by 3 different readers in 3 independent assays. Serum samples were dialyzed against phosphate buffered saline, and solutions were used at pH of 7.4. Sera were purified in order to extract IgG isotype antibodies and dialyzed against phosphate buffer saline. Immunoglobulins from three different patients were pooled together, whereas CSFs were kept separate. Written informed consent was obtained from all participating subjects.

Animal experiments
Animal procedures were conducted in accordance with the European Community guidelines (Directive 2010/63/EU) regulating animal research, and were approved by the local Bordeaux Ethics Committee (APAFIS #23521-2019120616502664). For *in vivo* experiments, 2-months old male Sprague-Dawley rats (Janvier, France) were used. Experiments were conducted during the light cycle (05:00 to 17:00) by the same experimenter who handled the animals throughout the whole duration of the experiment. Rats were kept at ambient temperature (21° ± 1°C) with *ad libitum* access to food and water. Every effort was made to minimize the number of animals used and their suffering. Rats were housed two by cage with the same litter and with the same treatment/cage. All animals were acclimatized to the room for at least 1 hour before the onset of each test. During open field and pre-pulse inhibition (PPI) tests, the experimenter was not blind to the animal's condition but behavioural data were collected using a computer-controlled system. The 86 rats (15 sham, 21 Healthy-IgG, 21 NMDAR-IgG, 11 NMDAR-IgG + KET, 9 Healthy-IgG + KET, 9 NMDAR-IgG + CPP) underwent surgery to implant a sub-cutaneous osmotic pump (200 μl) connected to an intracerebral catheter perfusing the right ventricle during 14 days. Behavioural tests were conducted following following a recovery period at 10 (sucrose preference), 14 (elevated plus maze), 15 (open field), 16 (novel object recognition), 17 (prepulse inhibition), and 18 (forced swim test) days after surgery. Animals were sacrificed at 21 days post-surgery and there brains were collected for further analysis. All drugs were dissolved in the same vehicle (sterile water).

Primary hippocampal cell cultures
Hippocampal cultures were prepared from embryonic day 18 Sprague-Dawley rat pups. Embryo brains were quickly removed and put in a dish with Leibovitz's L-15 medium. The hippocampus was isolated and incubated at 37°C for 15 min with a trypsin solution. Cerebral tissue was immersed in Hank's Balanced Salt Solution (HBSS) (KCl 5.33 mM, KH_2PO_4 0.44 mM, $NaHCO_3$ 4.16 mM, NaCl 137.93 mM, Na_2HPO_4 0.33 mM, D-Glucose 5.55 mM) (ThermoFisher Scientific) for dissection. The cell suspension - containing neurons and glia - was diluted in 60 mm sterile petri dishes containing pre-warmed Neurobasal culture medium supplemented with horse serum and poly-L-lysine coated 18 mm cover-slips, at a density of $250\text{-}275.10^3$ cells per ml. Dishes were maintained at 37°C in 5% CO_2 in a humidity-controlled incubator. For standard primary cultures, a full medium exchange with serum-free Neurobasal/B-27 culture medium was performed at 3 days *in vitro* (DIV). Full media exchanges continued twice weekly until use. For neuronal cultures

following the protocol of Kaech and Banker,[82] coverslips were flipped onto astrocyte feeder layers 3 hours after plating and maintained in this inverted configuration. At DIV 3, a full medium exchange with serum-free Neurobasal/B-27 culture medium containing 5 μM cytosine arabinoside was performed to prevent astrocyte proliferation. The protocol was used for experiments in which astrocytic expression of target surface proteins could interfere with data collection or add extraneous noise to imaging of neuronal cells.

METHOD DETAILS

Cerebroventricular infusions
Cerebroventricular infusions were performed using osmotic pumps (model 2002, Alzet®) with the following characteristics: volume 200 μl, flow rate 0.5 μl/h, and total duration 14 days. The day before surgery, osmotic pumps (one per animal) were loaded with 20 μl (100 μg) of human NMDAR-IgG or Healthy-IgG in presence or absence of 180 μl of KET hydrochloride (100 mg/ml, Virbac®, France) or CPP (0.8 mM final; Tocris Bioscience, UK). The saline control received 0.9% NaCl solution. The volume of KET hydrochloride was 180 μl, equivalent to a pump concentration of 380 mM. The pumps were then connected to a polyethylene tube (brain infusion kit2, Alzet®) and left 4h in sterile physiological serum at +4°C. Rats were anaesthetized by isoflurane inhalation and subcutaneously injected with buprenorphine (0.1 mg/kg) and meloxicam (1 mg/kg). They were placed on a stereotaxic frame, and after drilling the skull bone, the catheter was inserted into the right ventricle (0.9 mm anterior and 1.1 mm lateral from bregma, depth 0.32 mm). The arm of the catheter was connected to the osmotic pump which was subcutaneously implanted on the back. Appropriate ventricular placement of the catheters was assessed in randomly selected rat injecting methylene blue through the catheter. Twenty-one days following surgery, animals were anesthetized with pentobarbital (50 mg/kg) and transcardially perfused with 4% paraformaldehyde. Brains were removed and postfixed overnight at 4°C. For immunohistochemistry, 18 μm-thick coronal tissue sections were cut on a microtome-cryostat (Leica CM3050S), thaw-mounted onto adapted slides (superfrost ultra plus, Thermo Scientific Labs), and stored at -20°C until further processing.

Behaviour experiments

Sucrose preference test
The sucrose preference test was performed 10 days after surgery. On the four days before the test, two bottles of water, one with 2% sucrose and the other without, were placed in the cage. Every day the position of the bottles was exchanged and the consumption from each bottle was measured. On the day of the test, the two bottles were placed in the cage again and the consumption from each bottle was recorded after 24 h. The preference for sucrose was calculated as the relative amount of water with sucrose versus total liquid (water with and without sucrose) consumed by the rats.

Elevated plus maze test
The elevated plus maze test was performed 14 days after surgery. This test measures the conflict between the natural tendency of animals to avoid an illuminated and elevated surface, and their natural tendency to explore new environments. We used a rat elevated plus maze (Imetronic®, Pessac France) made of medium-density fiberboard with a matte grey acrylic surface, which consists of four arms (two open arms without walls and two arms enlosed by 30 cm-high walls) with the following dimensions: 50 cm long and 10 cm wide. The closed arms received a 10 lux light intensity whereas the open arms received 200 lux. Rats were placed at the junction of the open and closed arms, facing the open arm opposite to where the experimenter was located. The behaviour of each animal was tracked for 10 min and analysed using a video camera connected to a computer interface equipped with a video tracking software (EthoVision XT, Noldus®). The following parameters were monitored: time spent in open or in closed arms, entries made in open or in closed arms, and total entries made.

Open field test
The open field test was performed 15 days after surgery. The locomotor activity was measured in a homemade open field arena (54 long × 54 wide × 40 cm high) with light settings at approximately 20 lux. Novelty-induced locomotion was assessed by video tracking rats that freely explored the empty arena during 10 min. From the recordings, anxiety was evaluated as the time spent within a center zone comprising 50% of the arena during the first 10 min. Adaptation to context was assessed as a decrease in locomotor activity. The total distance travelled and velocity were tracked and analyzed using a video camera connected to a computer interface equipped with a video tracking software (EthoVision XT, Noldus®).

Novel object recognition test
The novel object recognition test was performed 16 days after surgery in a homemade open field arena (54 long × 54 wide × 40 cm high). Rats were placed into the open field arena for 10 min while two identical objects were presented and the time spent by the rat exploring each object was recorded. After a retention phase of 3 h, rats were placed for another 10 min into the open field arena but one of the familiar objects was replaced by a novel object and the total time spent exploring each object (novel and familiar) was registered. Objects were positioned in the opposite corners of those used in the training phase and the novel object was presented in 50% of trials on the right and in 50% of trials on the left side. Object exploration was defined as the orientation of the nose towards the object within a distance of less than 2 cm. A discrimination index was calculated as the difference between the time spent exploring the novel and the time spent exploring the familiar object divided by the total time exploring both objects. A higher discrimination index is considered to reflect better memory retention for the familiar object.

Neuron
Article

CellPress
OPEN ACCESS

Pre-pulse inhibition (PPI) test

The PPI test was performed using a Panlab startle chamber (Harvard Apparatus) 17 days after surgery. Each PPI session lasted for approximately 40 min and began with a 5 min acclimatization period with a constant background noise. The session consisted of 8 different trial types: a no pulse, a startle pulse (120 dB at 8 kHz, 40 ms) that was preceded by 3 prepulses at +4, +8, and +12 dB above a 74 dB background noise (20 ms, interval of 100 ms). Each session started with 10 startle pulses (intertrial intervals (ITIsec) of 70 s) followed by a counterbalanced pseudorandom order of the 8 trials × 6 and ended with a final block of 10 startle pulses. Baseline data from different groups were pooled. Potentiation in the response to the prepulses was observed in different animal groups, and these animals were excluded from the final dataset. Prepulse inhibition is expressed as % PPI and was calculated as $(100*((S - PP)/S))$, where S is the average response on startle only trials and PP is the average response on prepulse + startle trials.

Forced swim test

The forced swim test was performed 18 days after surgery to assess depressive-like behaviour. Rats were placed in a plastic cylinder containing warm water (27-28° C), deep enough to prevent touching the bottom of the cylinder and forcing the rats to swim. The trial lasted 5 min and the total time of immobility after 2 min was recorded. Immobility was defined as the time that the animal stopped swimming and only used minimal movements to keep the head above the water.

Z-score calculations

As previously described,[83] z-scores were calculated as a set of converging behavioral observations. The z-score represent the value for each animal minus the mean of the control group, divided by the standard deviation of the control group. The z-score for anxiety/depression-like behavior was calculated as the mean of z-scores of each animal taking into consideration the sucrose preference test (index sweet water/total water consumption: percentage of sucrose preference), the elevated plus maze test (index open/closed arms: percentage of time in open arms), the open field test (percentage of time spent in the center zone) and the forced swim test (percentage of time spent immobile). The z-score for locomotor activity was calculated as the mean of z-scores of each animal taking into consideration the horizontal activity (distance covered during 10 min) and the velocity (average velocity over 10 min) in the open field test.

Transfection

For live imaging experiments, cultured hippocampal neurons were transfected at days in vitro (DIV) 7-10 using the calcium-phosphate method. Precipitates containing 1 mg plasmidic DNA (see key resources table) were prepared using the following solutions: TE (1 M Tris-HCl pH 7.3, 1 mM EDTA), $CaCl_2$ (2.5 M $CaCl_2$ in 10 M HEPES, pH 7.2), 2X HEPES-buffered saline (HEBS; 12 mM dextrose, 50 mM HEPES, 10 mM KCl, 280 mM NaCl and 1.5 mM Na_2HPO_4-$2H_2O$, pH = 7.2). Coverslips were transferred to 12-well plates containing 250 μl/well of conditioned culture medium supplemented with 2 mM kynurenic acid (Sigma-Aldrich), and 50 μl of DNA precipitate solution was added to each well. Cells were incubated for 1 h at 37°C, then washed with unsupplemented Neurobasal medium containing 2 mM kynurenic acid and moved back to their original culture dishes. Transfection was monitored following at least 3 days.

Immunostaining

Cultured hippocampal neurons from E14 rat embryos were plated at a density of 2.75-3.25 x 105 neurons/mL in 60 mm Petri dishes containing 18 mm glass coverslips pre-coated with poly-L-lysine (Sigma-Aldrich). Neurons were maintained at 37°C and 5% CO_2 for up to 21 days. A 3% Horse Serum (ThermoFisher Scientific) solution was present in the culture medium until 4-7 days in vitro (DIV). Neurons were cultured in Neurobasal™ medium (ThermoFisher Scientific) supplemented with NeuroCult™ SM1 (Stemcell technologies). Progressively, Neurobasal was partially replaced with equally supplemented BrainPhys™ medium (Stemcell technologies). Cultured neurons at DIV 13-15 were incubated 6-12 h with human control or NMDAR-IgG at 37°C with or without NMDAR antagonists. Surface exogenous flag-GluN1 NMDAR were immunostained in live neurons using a mouse monoclonal anti-flag antibody (Sigma-Aldrich; 10 min at 37°C). Neurons were then fixed in 4% PFA for 15 min at room temperature. Fixed samples were carefully washed and immersed in a PBS 1X-NH_4Cl 50 mM quenching solution for 10 min. Samples were subsequently labeled for 1h with an anti-mouse Alexa 647-conjugated secondary antibody (ThermoFisher Scientific; 1/500) in a PBS 1X-BSA 1% blocking solution. Coverslips were carefully washed again and mounted onto glass slides with Mowiol mounting medium (composed of: Mowiol 4-88 9.6% (w/v), Glycerol 24% (w/v), and Tris-Cl (0.2 M, pH 8.5) 0.1 M). Surface endogenous GluN2B, exogenous SEP-GluN2A or SEP-GluN1 NMDAR were specifically immunostained using a monoclonal antibody against GluN2B (Alomone Labs, 1/500, 12 min, 37°C; homemade antibodies 2 mg/ml, Agro-Bio Labs, 1:20) or against GFP for SEP-containing subunits (Roche Labs, 1/500, 12 min, 37°C). Primary antibodies were incubated for 2 h followed by secondary staining with Alexa 488-conjugated anti-mouse secondary antibody (Invitrogen, 1/500, 30 min). In order to label the post-synaptic density, neurons were fixed (4% PFA, 15 min), permeabilized with Triton-BSA 1% (5 min) and successively incubated with anti-Homer1c antibody (Synaptic Systems; 1:500, 30 min) and a secondary anti-guinea pig Alexa 594 antibody (Jackson ImmunoResearch, 1/500, 30 min). Fluorescence acquisitions were performed using a Yokogawa CSU-X1 spinning-disk system (Yokogawa Electric Corporation, Tokyo, Japan) mounted on a Leica DMI6000B microscope (Leica Microsystems, Wetzlar, Germany). Samples were excited using a diode-pumped solid-state 491 laser (200 mW, 8.5-10% power, 100-200 ms exposure time) and a 642-laser diode (100 mW, 7-7.5% power, 500 ms exposure time). Images were acquired using a Plan Apo 63x oil immersion objective (NA 1.4-0.6), the appropriate excitation/emission filters and an Evolve

EMCCD camera (Teledyne Photometrics). An initial experiment (1 out of 4) was p/rformed using a coolSNAP HQ2 CCD camera (Teledyne Photometrics), a Plan Apo 100x oil immersion objective (NA 1.4-0.7), and diode-pumped solid-state 491 (100 mW, 30% power, 700 ms exposure time) and 642 (50 mW, 50% power, 800 ms exposure time) lasers. 10-15 cells per condition from independent experiments were selected. From each neuron, only one dendrite was chosen for fluorescence quantification analysis. Images were subjected to a user-defined intensity threshold for cluster selection and background subtraction. The mean fluorescence intensity was measured for all clusters of the selected region. Synaptic clusters were determined as overlapping thresholded Homer1c clusters. All analyses were done blind to treatment condition. For surface cluster analysis, dendritic branches were chosen manually in a blinded manner and cluster areas and numbers were obtained using a manual threshold approach based on integrated fluorescence levels in ImageJ (NIH).

Calcium imaging

Dissociated hippocampal neurons were transfected with GCaMP6f and DsRed-Homer1c between DIV 8 and 10 using the calcium-phosphate coprecipitation method. On the day of experiment (DIV 15-19), coverslips were transferred to a RC-41LP recording chamber (Harvard Apparatus; Cat# 64-0368). Cells were maintained in a pre-heated and equilibrated (37 °C / 5% CO_2) Tyrode solution composed of the following (in mM): 110 NaCl, 5 KCl, 2 $MgCl_2$, 2 $CaCl_2$, 15 D-Glucose, 25 HEPES (pH 7.4; 276 mOsm). Three time-lapse movies (3,000 frames, 20 Hz frame rate) were successively recorded on a widefield Nikon eclipse Ti microscope (Nikon France) equipped with a Plan Apo 60X oil immersion objective (NA 1.40) using a mercury lamp, appropriate excitation/emission filters and an Evolve EMCCD camera (Teledyne Photometrics). Cells were imaged before (baseline) and after being exposed to NMDA combined with either D-AP5 (50 μM), MK-801 (20 μM), KET (1 μM) or MEM (1 μM) for 5 min. D-AP5 was then added in the imaging chamber for 5 min to obtain a baseline recording free of NMDAR-dependent calcium transients. Dendritic spines were visually identified using DsRed-Homer1c signal to avoid bias towards more active spines, and average fluorescence (F) values for each spine were recorded over time. Time-lapse movies were concatenated and realigned in ImageJ (PoorMan3DReg plugin, Michael Liebling, and Template Matching plugin, Qingzong Tseng). Fluorescence from calcium transients vs. time was measured within individual ROIs manually defined by the experimenter (ImageJ, NIH). All pixels within each ROI were averaged to give a single value time course associated to the ROI. Mean normalized fluorescence ($\Delta F/F$) was calculated by subtracting each value with the mean of the previous 5 s values lower than P_{50} (μ) and dividing the result by μ. Positive calcium transients were identified following a two-step procedure: initially, $\Delta F/F$ traces were smoothened by convoluting the raw signal with a 10 s squared kernel. True positives (with minimal intervals of 1s between transients) were then defined on an automated basis using custom-written MATLAB (MathWorks) routines where the threshold was set at 5 times the standard deviation of the corresponding D-AP5 average trace.

Photo-activated localization microscopy (PALM)

Dissociated hippocampal neurons were prepared from E18 Sprague-Dawley rats and plated on 18 mm poly-lysine-pre-coated coverslips, as previously described.[17] Neurons were transfected with mEos3.2-GluN1 and GFP-Homer1c between DIV 8 and 10 using the calcium-phosphate coprecipitation method. On the day of experiment (DIV 14-15), coverslips were mounted on a Ludin chamber (Life Imaging Services). Cells were maintained in a pre-heated and equilibrated (37 °C / 5% CO_2) Tyrode solution composed of the following (in mM): 108 NaCl, 5 KCl, 2 $MgCl_2$, 2 $CaCl_2$, 15 D-Glucose, 25 HEPES (pH 7.4; 276 mOsm). Image acquisitions were performed on a Nikon Ti-Eclipse microscope (Nikon France) equipped with an incubator box and an air heating system (Life Imaging Services), a Perfect Focus System (PFS), a motorized stage TI-S-ER, and an azymuthal Ilas[2] TIRF arm (Gataca Systems) coupled to a laser bench containing 405 nm (100 mW), 488 nm (150 mW), 532 nm (1 W), 561 nm (200 mW) and 642 nm (1 W) diodes. Photo-conversion of mEos3.2 was achieved using the 405 nm laser and photo-converted single molecule fluorescence was excited with the 561 nm laser. Both lasers illuminated the sample simultaneously and their respective powers were adjusted to maintain the number of stochastically-activated molecules constant during acquisitions. The angle of illumination was adjusted in oblique configuration to detect mEos3.2 signals at the cell surface and to decrease background noise. Fluorescence signals were detected using an Apo TIRF 100X NA 1.49 oil-immersion objective and a Fusion BT sCMOS camera (Hamamatsu Photonics). The microscope and image acquisition were driven by the Metamorph software (Molecular Devices). Redistributions of mEos3.2-GluN1 at the neuronal surface were monitored for 4000 frames at 20 Hz acquisition rate (200 s recordings). Each neuronal field was imaged twice, i.e. before and after a 5 min exposure to NMDA (5 μM) alone or combined with either D-AP5 (50 μM), KET (1 μM), MK-801 (20 μM) or memantine (1 μM). Drugs were added directly into the bath after the first acquisition. Trajectory reconstruction and data extraction were performed using the PALMTracer plug-in running under the Metamorph software environment (J.B. Sibarita, Bordeaux). The two-dimensional trajectories of single molecules in the plane of focus were constructed by correlation analysis between consecutive images using a Vogel algorithm. For each trajectory, the instantaneous diffusion coefficient 'D' was calculated from linear fits of the first 4 points of the mean-square-displacement versus time function using MSD(t) = <r2> (t) = 4Dt. Synaptic areas were defined by wavelet image segmentation from fluorescence images of the GFP-Homer1c postsynaptic marker.

Direct Stochastic Optical Reconstruction Microscopy (dSTORM)

Dissociated hippocampal neurons were transfected with GFP-Homer1c and Flag-GluN1 between DIV 8 and 10 using the calcium-phosphate coprecipitation method. On DIV 14-17, neurons were exposed to TTX (1 μM), D-AP5 (50 μM), KET (1 μM), MK-801 (20 μM) or MEM (1 μM) for 1h. Neurons were then incubated with blocking agents (HEPES 10 mM, BSA 1%; 5 min, 37°C) and labeled using a

CellPress
OPEN ACCESS

mouse monoclonal anti-Flag antibody (Sigma-Aldrich, Saint-Louis, MO, USA, Cat# N° F1804, 1/500, 10 min, 37°C) in the presence of different drugs. Samples were fixed in 4% PFA (15 min, RT) and carefully washed in a quenching solution (PBS-1X, NH$_4$Cl 50 mM). Unspecific antibody binding sites were masked using a blocking solution (1.5% BSA, 0.1% fish gel, 0.1% Triton-100X; 45 min, RT). Samples were labeled with an anti-mouse Alexa 647-conjugated secondary antibody (ThermoFisher Scientific, 1/500; 1h, RT). Coverslips were carefully washed and stored in PBS 1X at 4°C until imaging. Multicolor fluorescent TetraSpeck™ microspheres were added to the samples before image acquisition (ThermoFisher Scientific, Cat# T7279; 1/500; 10 min, at RT). Imaging sessions were performed on a Nikon Eclipse Ti microscope (Nikon France) equipped with a Perfect Focus System (PFS), an azymuthal Ilas^2 TIRF arm and scanner system (Gataca Systems), a Ti-S-ER motorized stage controlled by MetaMorph software (Molecular Devices), an Apo TIRF 100X oil-immersion objective (NA 1.49) and an Evolve EMCCD camera (Teledyne Photometrics) with a final pixel size of 160 nm. Alexa 647 fluorophores were converted into the dark state using a 642 nm fiber laser at maximum power (1,000 mW), and a stable optimized rate of stochastically-activated molecules per frame was achieved by controlling the power of a diode-pumped solid-state 405 nm laser (1,000 mW) while fixing the 642 nm laser power to around 30% of maximum. Samples were illuminated in TIRF mode and images were obtained with an exposure time of 20 ms (50 Hz frame rate) up to 80,000 consecutive frames. Imaging was carried out at RT in a closed Ludin chamber (Life Imaging Services) using a pH-adjusted extracellular solution containing oxygen scavengers and reducing agents.[84] Single-molecule localization and reconstruction was performed online with automatic feedback control of the lasers using the WaveTracer module, enabling optimal single-molecule density during the acquisition.[78] The acquisition and localization sequences were driven by MetaMorph software in streaming mode using a region of interest of 256 x 256 pixels. Super-resolved images were reconstructed with the PALMTracer software plugin for MetaMorph using a Gaussian fit (xy sigma) to determine the centroid-coordinates of a single molecule and lateral drift correction was achieved using the positions of the photostable TetraSpeck™ beads. SR-Tesseler software was used to quantify protein clustering from the detected fluorophore coordinates.[79] This method uses a Voronoi diagram to decompose a super-resolved image into polygons of various sizes, which are drawn by equally dividing the distances between all adjacent detections. From those polygons, several parameters can be extracted, such as the first-rank density σi^1 of a detected molecule i. Automatic segmentation of clusters was performed by selecting sets of detections having a density σi^1 higher than $2\sigma^d$, with σ^d being the average density of a user-defined region (containing one dendrite). All selected neighboring molecules were merged and only clusters having a minimum area of 1.25 px^2 (minimum area of 180 nm^2 based on the size of GluN1 clusters in epifluorescence) and a minimum number of localizations of 5, as previously defined.[8] were considered. For each cluster j, automatic segmentation of the nanodomains was achieved by applying $\sigma_{(i,j)}^1 > 1\sigma_j^o$, with σ_j^o the average density of the cluster j and $\sigma_{(i,j)}^1$ the density of its ith molecule. As for clusters, all selected neighboring molecules were merged and only nanodomains having a minimum area of 0.00625 px^2 (minimum area of 12.65 nm^2 based on the size of an NMDAR) and a minimum number of localizations of 25 based on the number of times a single emitter is expected to blink during the total length of an acquisition were considered.[8] Size parameters of both the clusters and the nanodomains were extracted by principal component analysis. Local detection densities were calculated as the number of localizations divided by the respective area of the cluster or nanodomain. Synaptic NMDAR clusters were identified manually by superimposing an epifluorescence image of GFP-Homer1c to a super-resolved image of Flag-GluN1 clusters.

Fluorescence recovery after photobleaching (FRAP)

Dissociated hippocampal neurons were transfected with SEP-GluN2A between DIV 8 and 10 using the calcium-phosphate coprecipitation method. On DIV 14-16, neurons were exposed to NMDAR-IgG, with or without KET (10 μM) or D-AP5 (50 μM) for either 20 min or 12 h, and were subsequently imaged on an inverted confocal Leica DMI6000B microscope (Leica Microsystems) with a Yokogawa CSU-X1 spinning-disk system (Yokogawa Electric Corporation). Acquisitions were performed using a Plan Apo 63x oil immersion objective (NA 1.4) and a Prime 95B camera (Teledyne Photometrics, Tucson, AZ, USA). A 488 nm laser (400 mW) at 50% intensity was used to photobleach locally. Recovery from photobleaching was monitored by three consecutive acquisition periods at 2, 0.5, and 0.1 Hz acquisition rates, respectively, using the appropriate excitation/emission filters. Clusters were imaged over a period of 180 s. Fluorescence intensity was measured using MetaMorph software (Molecular Devices) and corrected for acquisitional photobleaching. Image analysis and background noise were performed using homemade plugins in ImageJ (NIH).

Frequency domain based fluorescence lifetime imaging microscopy of Förster resonance energy transfer (FLIM-FRET)

Dissociated hippocampal neurons were transfected between DIV 8 and 10 using the calcium-phosphate precipitation method. For experiments designed to probe NMDAR conformational rearrangements elicited by antagonists or antibodies, neurons were co-transfected to express recombinant NMDAR complexes incorporating C-terminus-tagged GluN1-GFP (donor fluorophore) and GluN1-mCherry (acceptor fluorophore; gifts from Paul de Koninck) together with flag-tagged GluN2B subunits (gift from Robert Wenthold), as previously described.[31,85] Causality between drug binding to the receptor and changes in conformation was tested by expressing GluN1-N616A-GFP and GluN1-N616A-mCherry incorporating a point mutation within the binding site for KET.[33] For intermolecular FRET experiments designed to assess whether antagonists affect interactions between NMDAR and MAGUKs, neurons were co-transfected to express GluN1-GFP (donor fluorophore) and PSD-95-mCherry (acceptor fluorophore; gifts from Paul de Koninck).[32] For intramolecular FRET experiments designed to explore if KET would prevent NMDAR-IgG-elicited impairments in CaMKIIα activity, neurons were transfected to express the FRET-based sensor Green-Camuiα in which the N- and

CellPress
OPEN ACCESS

Neuron
Article

C-termini of CaMKIIα are labelled with monomeric enhanced GFP (mEGFP, donor fluorophore) and resonance energy-accepting chromoprotein (REACh, acceptor fluorophore), respectively.[38] On the day of experiment (DIV 12-15), coverslips were mounted on a Ludin chamber (Life Imaging Services, Basel, Switzerland). Cells were maintained in a pre-heated and equilibrated (37 °C / 5% CO_2) Tyrode solution composed of the following (in mM): 108 NaCl, 5 KCl, 2 $MgCl_2$, 2 $CaCl_2$, 15 D-Glucose, 25 HEPES (pH 7.4; 276 mOsm). Image acquisitions were performed at 37°C on an inverted Leica DMI6000B microscope (Leica Microsystems) equipped with an incubator box and an air heating system (Life Imaging Services), a Yokogawa CSU-X1 spinning-disk system (Yokogawa Electric Corporation, Tokyo, Japan), a motorized stage controlled with MetaMorph software (Molecular Devices, Sunnyvale, USA), and using a LIFA frequency domain lifetime attachment and the LI-FLIM software (Lambert Instruments BV). Cells were excited using a sinusoidally modulated (36 MHz) 478 nm LED (1 W) under wide-field illumination. Emissions were collected using HCX Plan Apo CS 63X (NA 1.4) or HCX Plan Apo 100X (NA 1.4) oil immersion objectives, an appropriate filter set and an intensified Li2CAM CCD camera (Lambert Instruments BV, Groningen, The Netherlands). Lifetimes were calibrated using a solution of erythrosin B (1 mg/ml) as a reference (0.086 ns; 30 ms exposure time). GFP lifetimes of the samples were determined from the fluorescence phase-shift between the sample and the reference from a set of 12 phase settings using LI-FLIM software (Lambert Instruments BV). FRET efficiency was calculated as EFRET = 1 - (τ_{DA}/τ_D), where τ_{DA} is the lifetime of the donor fluorophore (GFP) in the presence of the acceptor (mCherry) and τ_D is the average lifetime of the donor alone, as previously described.[32] Depending on experimental configurations, neuronal fields were selected based on the expression of GluN1-GFP, GluN1-N616A-GFP, Green-Camuiα, GluN1-mCherry, GluN1-N616A-mCherry and PSD-95-mCherry which were excited using either 491 nm (GFP) or 561 nm (mCherry) diode lasers (100 mW). Fluorescence signals were visualized using an appropriate filter set and an Evolve EMCCD camera (Teledyne Photometrics), and acquisitions were carried out using MetaMorph. GFP lifetimes were measured using the LI-FLIM software from 20 to 30 dendritic spines manually defined using ImageJ (NIH) based on the presence of GluN1-GFP and GluN1-mCherry clusters, blind to the FLIM image. In experiments probing NMDAR conformational rearrangements elicited by antagonists, each neuronal field was imaged twice, i.e. before and 5 min after exposure to NMDA (5 μM) alone or combined with either D-AP5 (50 μM), KET (1 μM), MK-801 (20 μM) or MEM (1 μM). Drugs were added directly into the bath after the first acquisition. To explore the contribution of interactions between NMDAR and MAGUKs in KET-induced conformational rearrangements, neurons were pre-incubated for 1h either with a nonsense (TAT-NS; YGRKKRRQRRRGSEVILDQPVIAKPLIPALSVALSVKEEA, 10 μM; CASLO ApS, Kongens Lyngby, Denmark) or a biomimetic peptide (TAT-2B; YGRKKRRQRRRNGHVYEKLSSIESDV, 10 μM) competing with GluN2B for the binding to PDZ domains.[35] GFP lifetimes were acquired in the presence of the peptides before and 5 min after application of NMDA (5 μM) together with KET (1 μM). The ability of KET to compensate for antibody-elicited conformational rearrangements in NMDAR cytosolic domains was probed through repeated measures of GFP lifetime. After a first acquisition in Tyrode medium, Healthy-IgG or NMDAR-IgG were added to the bath and incubated for 15 min before a second acquisition was performed. KET (10 μM) was then added to the bath for 15 min and a third measurement was achieved. Repeated measures of GFP lifetime were also implemented with the Green-Camuiα FRET-based sensor to assess the ability of KET and D-AP5 to prevent NMDAR-IgG-elicited impairments in CaMKIIα activity. Prior to imaging, cells were pre-incubated for 1h with either buffer, KET (10 μM), D-AP5 (50 μM), Healthy-IgG, NMDAR-IgG, or NMDAR-IgG combined with KET or D-AP5. GFP lifetimes were then acquired every minute before (two baseline timepoints) and after addition of glutamate (25 μM) to the bath to stimulate NMDAR-mediated recruitment of CaMKIIα activity.

Single particle tracking (SPT)

Single particle tracking of endogenous or recombinant NMDAR, γ2-GABA$_A$R, EphB2R and K$_V$1.3 was performed as previously described.[17] For experiments involving recombinant proteins, neurons were transfected between DIV 8 and 10 to express SEP-γ2, Flag-GluN2A-WT, Flag-GluN2B-WT, Flag-GluN2A-S1462A, Flag-GluN2B-S1480A or SEP-GluN2A using the calcium-phosphate coprecipitation method. DsRed-Homer1c and mVenus-Gephyrin were expressed as exogenous markers of excitatory and inhibitory synapses, respectively. On DIV 13-15, dissociated hippocampal neurons were incubated for 10 min (37°C, 5% CO2) with polyclonal antibodies against either GluN1 (rabbit; Alomone Labs; 1:200), EphB2R (goat; R&D systems; 1:200), K$_V$1.3 (rabbit; Alomone Labs; 1:200), GFP (rabbit; ThermoFisher Scientific; 1:50,000) or Flag (rabbit; Sigma-Aldrich, 1:10,000). Neurons were then washed and incubated for 10 min with either F(ab')2-goat anti-rabbit IgG (H+L) secondary antibody, Qdot 655 (ThermoFisher Scientific; 1:10,000) or F(ab')2-rabbit anti-goat IgG (H+L) secondary antibody, Qdot 655 (ThermoFisher Scientific; 1:10,000). Non-specific binding was blocked by adding 1% BSA (Sigma-Aldrich) to the labelling solutions. All incubations were performed in pre-heated Tyrode solution containing (in mM): 110 NaCl, 5 KCl, 2 MgCl2, 2 CaCl2, 12 D-glucose, 25 HEPES, pH 7.4, 1% BSA. Coverslips were transferred to a RC-41LP recording chamber (Harvard Apparatus; Cat# 64-0368) and perfused with pre-heated and equilibrated (37 °C / 5% CO_2) Tyrode medium. Drugs, peptides and antibodies were either pre-incubated or added directly into the bath, as indicated. Image acquisitions were performed on a Nikon Ti-U Eclipse microscope (Nikon France). QD were detected using a mercury lamp and appropriate excitation/emission filters. Images were acquired using an exposure time of 50 ms (20 Hz) with up to 500 consecutive frames. Signals were detected using an Evolve EMCCD camera (Teledyne Photometrics) controlled by MetaMoprh software (Molecular Devices). Tracking was performed on randomly-selected dendritic regions for up to 20 min. The instantaneous diffusion coefficient 'D' was calculated for each trajectory, from linear fits of the first 4 points of the mean-square-displacement versus time function using MSD(t) = <r2> (t) = 4Dt. The two-dimensional trajectories of single molecules in the plane of focus were constructed by correlation analysis between consecutive images using a Vogel algorithm.

QUANTIFICATION AND STATISTICAL ANALYSIS

Sample sizes were determined based on previous studies using similar experimental paradigms. For behaviour experiments, a predetermined sample size was based on previous studies and the literature.[39,86] A sample size of 10 to 15 rats was used, which corresponds to a power factor of 0.6. The number of replicates for each experimental group is listed in the figure legends, with N representing the number of cells and n representing the number of trajectories for SPT and PALM experiments, the number of clusters for FRET and immunostaining experiments, the number of clusters or nanordomains for STORM experiments, the number of dendrites for spine counting experiments, the number of ROIs for FRAP experiments, and the number of animals for behaviour experiments, respectively. All statistical analysis was performed in GraphPad Prism (version 9.2, GraphPad Software Inc., San Diego, USA). A D'Agostino and Pearson omnibus normality test was applied to determine the normality of the data. For normally distributed data, the following parametric tests were applied: for unpaired data, Student t-test; for paired data, paired t-test test; for unmatched grouped data, one-way ANOVA followed by Tukey's multiple comparison test. For data that did not follow a normal distribution, the following non-parametric tests were applied: for unpaired data, Mann-Whitney test; for paired data, Wilcoxon matched-pairs signed rank test; for unmatched grouped data, Kruskal-Wallis test followed by Dunn's multiple comparison test. For distribution comparisons, a Kolmogorov-Smirnov test was used. In all cases, differences were considered significant at $p<0.05$. Statistically significant differences between conditions are represented as asterisks ($p>0.05$, $*p<0.05$, $**p<0.01$, $***p<0.001$). Figures were assembled in ImageJ (NIH), only contrast and brightness were adjusted to optimize the image quality.